Gradients of Recognition Molecules Shape Synaptic Specificity of a Visuomotor Transformation

Mark Dombrovski[1], Yixin Zang[2#], Giovanni Frighetto[3#], Andrea Vaccari[4#], Hyojong Jang[5#], Parmis S. Mirshahidi[1#], Fangming Xie[1], Piero Sanfilippo[1], Bryce W. Hina[5], Aadil Rehan[1], Roni H. Hussein[1], Pegah S. Mirshahidi[1], Catherine Lee[1], Mark A. Frye[3], Catherine R. von Reyn[5], Yerbol Z. Kurmangaliyev[6], Gwyneth M. Card[2*] & S. Lawrence Zipursky[1*]

[1]Department of Biological Chemistry, David Geffen School of Medicine, University of California, Los Angeles, Los Angeles, CA, USA
[2]Department of Neuroscience, Howard Hughes Medical Institute, The Mortimer B. Zuckerman Mind Brain Behavior Institute, Columbia University, New York, NY, USA
[3]Department of Integrative Biology and Physiology, University of California, Los Angeles, Los Angeles, CA, USA
[4]Department of Computer Science, Middlebury College, Middlebury, VT, USA
[5]School of Biomedical Engineering, Science and Health Systems, Drexel University, Philadelphia, PA, USA
[6]Department of Biology, Brandeis University, Waltham, MA, USA

[#]Equal contributions

*Correspondence: S. Lawrence Zipursky (lzipursky@mednet.ucla.edu), Gwyneth M. Card (gc3017@columbia.edu),

Abstract

Converting sensory information into motor commands is fundamental to most of our actions[1,2]. In *Drosophila*, visuomotor transformations are mediated by Visual Projection Neurons (VPNs)[3,4]. These neurons convert object location and motion into directional behaviors downstream through a synaptic gradient mechanism[5]. However, the molecular origins of such graded connectivity remain unknown. We addressed this question in a VPN cell type called LPLC2[6], which integrates looming motion and transforms it into an escape response through two parallel dorsoventral synaptic gradients at its inputs and outputs. We identified two corresponding dorsoventral expression gradients of cell recognition molecules within the LPLC2 population that regulate this synaptic connectivity. Dpr13 determines synaptic outputs of LPLC2 axons by interacting with its binding partner DIP-ε expressed in the Giant Fiber, a neuron that mediates escape[7]. Similarly, beat-VI regulates synaptic inputs onto LPLC2 dendrites by interacting with Side-II expressed in upstream motion-detecting neurons. Behavioral, physiological, and molecular experiments demonstrate that these coordinated molecular gradients control differential synaptic connectivity, enabling the accurate transformation of visual features into motor commands. As within-neuronal-type continuous variation in gene expression is also observed in the mammalian brain[8], graded expression of cell recognition molecules may represent a common mechanism underlying synaptic specificity.

Main

Every day, we engage in a multitude of visually guided behaviors that rely on the conversion of an object's location in eye coordinates into directional body movements[9,10]. The brain regions and neural circuits responsible for these visuomotor transformations have been characterized in both vertebrates[11–13] and invertebrates[14,15]. These studies have revealed that learned visuomotor tasks[16–18] and innate visuomotor responses[19,20] rely on precise neuronal connectivity, which is established during development, or through experience-dependent circuit plasticity.

In the fly brain, visuomotor transformation occurs between Visual Projection Neurons (VPNs) and Descending Neurons[21] (DNs, Fig. 1a). Although VPNs encompass a broad range of neurons that connect the optic lobe to the central brain[22], here we focus on well-characterized VPN sub-classes of columnar neurons[4], including LC (lobula columnar) and LPLC (lobula plate/lobula columnar). There are about 30 VPNs of these types, each comprising 20 to 200 neurons per brain hemisphere[3,4]. For simplicity, we will refer to these collectively as VPNs. The dendrites of individual neurons within a VPN type each span 20 to 40 degrees of visual space, and as a population, they uniformly cover the optic lobe (Fig. 1a), creating a feature-detecting retinotopic map[23–25]. The axon terminals of each VPN type bundle together in the central brain, forming optic glomeruli, where some elaborate synapses onto the dendrites of DNs. For most of the VPN types, axonal retinotopy is lost[4,5]. We recently demonstrated that the transformation from visual input to motor output in VPN-DN circuits relies on a synaptic gradient mechanism, which functions independently of axonal retinotopy[5].

We define a synaptic gradient as a connectivity pattern in which the number of synapses connecting individual neurons within a presynaptic population (e.g., a VPN type) to postsynaptic targets (e.g., DNs), exhibits a retinotopically biased systematic variation. For example, we found that within a population of looming-responsive VPNs, those with anterior receptive fields make more synapses onto DNs that drive backward movements, while neurons with posterior receptive fields make more synapses onto DNs that drive forward movements and takeoff[5]. This anterior-posterior gradient of synapses enables the fly to detect looming threats and execute a rapid escape response[5]. Thus, the synaptic gradient mechanism provides a non-spatial, abstract representation of visual space, serving as an example of retinotopically guided, yet spatially independent, within-cell-type synaptic specificity. While cell recognition molecules have been described that regulate synaptic specificity between different neuronal types[26–28], how neurons of the same type form varying numbers of synapses with their targets remains unclear.

To uncover the molecular basis of synaptic gradients, we focused on a specific type of VPN called lobula plate/lobula columnar 2 (LPLC2), a population of about 100 neurons per hemibrain, that each respond selectively to dark, radially-expanding motion stimuli centered on their receptive field, and, therefore act as local looming detectors[6,23]. The axons of LPLC2 neurons convey visual information to the Giant Fiber (GF), a DN that elicits a rapid escape takeoff in response to looming threats[7,29,30] (Fig. 1b). In our previous work, we analyzed electron

139 microscopy (EM)-based connectomic reconstructions from two brain volumes
140 (Janelia "hemibrain[31]" and "FAFB-Flywire[32,33]") and showed that LPLC2 neurons
141 elaborate a dorsoventral (DV) gradient of synapses onto the GF. Specifically,
142 LPLC2 neurons with dendrites sampling the dorsal part of the visual field form
143 more synapses with the GF than their ventral counterparts (Fig. 1c-d).
144 Here, we investigated the molecular basis of the LPLC2-GF synaptic
145 gradient by combining single cell RNA sequencing (scRNA-seq), spatial
146 transcriptomics and genetics with morphological, behavioral, and physiological
147 studies. We identified two cell recognition molecules expressed in a gradient
148 across the LPLC2 population. One of them, dpr13, regulates connections of LPLC2
149 axons and the GF dendrites. We also discovered a second recognition molecule,
150 beat-VI, which controls the formation of a synaptic gradient onto the dendrites of
151 LPLC2 neurons. This shows that varying levels of cell recognition molecules within
152 a defined neuronal type can specify different numbers of synapses both pre- and
153 post-synaptically. Our findings represent a new mechanism of regulating synaptic
154 specificity.
155

156 LPLC2-Giant Fiber Synaptic Gradient Shapes Escape Behavior

157 To determine whether the DV synaptic gradient between LPLC2 and the GF
158 is functional, we quantified the escape response to looming stimuli from different
159 parts of the visual field. Previous work showed that flies exhibit two modes of
160 takeoff – a short mode using only leg extension, and a long mode using
161 coordinated wing depression and leg extension[34] – and that short-mode takeoffs
162 result solely from activation of the GF[7]. We therefore predicted that if LPLC2
163 neurons with more dorsal receptive fields made more synapses with the GF than
164 ventral LPLC2 neurons, then we should observe more short-mode takeoffs in
165 response to higher, compared to lower, elevations of a looming stimulus. To test
166 this hypothesis, we analyzed thousands of previously collected[35] high-speed
167 videos of takeoffs elicited by looming stimuli at different elevations to determine
168 whether takeoff responses were short- or long-mode. As predicted, we found that
169 the percentage of short-mode takeoffs steadily increased as the elevation of the
170 looming stimulus increased from -30° to 77° (Fig. 1e, Extended Data Fig. 1a), as
171 would be expected from higher engagement of the GF in response to more dorsal
172 looming. Because the GF receives direct visual input from only one other VPN type
173 (LC4[36]) in addition to LPLC2, and LC4 neurons do not form a DV synaptic gradient
174 with the GF[5], the most parsimonious interpretation of our analysis is that this bias
175 toward short-mode takeoffs when looming occurs in the dorsal visual field results
176 directly from the synaptic gradient between LPLC2 and the GF. This bias
177 potentially enables the fly to escape more quickly from overhead predator attacks.
178 LPLC2 forms synaptic gradients without axonal retinotopy[4,5,37]. This means
179 dendrites of the GF establish differential connectivity with axons of different
180 individual LPLC2 neurons that are intermingled (Fig. 1f). We hypothesized that this
181 pattern could be achieved through differential molecular recognition: individual
182 LPLC2 neurons sampling different regions of visual space could express different
183 levels of the same cell recognition molecules. This mechanism would specify the

184 number of LPLC2-GF synapses independent of the spatial arrangement of LPLC2
185 axons.
186

187 scRNA-seq Uncovers Molecular Heterogeneity in VPNs

188 To investigate whether LPLC2 neurons exhibit molecular variation that
189 correlates with the synaptic gradient, we examined the LPLC2 transcriptome at
190 three developmental stages during and after synaptogenesis (48, 72, and 96 hours
191 after puparium formation (hAPF); Fig. 1g). In addition to LPLC2, we profiled its
192 sister cell type, LPLC1, which also forms synaptic gradients without axonal
193 retinotopy[5], and LC4, one of the few VPN cell types with axons arranged in a
194 retinotopic fashion[5]. Given that neuronal transcriptomes are very dynamic during
195 development and can be affected by genetic background[38], we introduced internal
196 controls at each time point to account for transcriptional heterogeneity driven by
197 these factors (Fig. 1g).
198 Briefly, we employed a genetic multiplexing strategy to perform pooled
199 single-cell profiling across multiple biological replicates[38–40] (including different
200 genetic backgrounds and developmental stages, see Methods). Our final dataset
201 included approximately 600 high-quality single-cell transcriptomes per cell type
202 and time point (Fig. 1h, Extended Data Fig. 1b). We validated the identity of each
203 VPN cell type (LPLC2, LPLC1, or LC4) based on the expression of known marker
204 genes[38], such as transcription factors (Fig. 1i, Extended Data Fig. 1b). This
205 resulted in per-cell-type coverage roughly 30 times higher than in the existing
206 single-cell atlases of the *Drosophila* optic lobes[38,41].
207 To explore heterogeneity in gene expression across each VPN cell type, we
208 performed Principal Component Analysis (PCA) separately for each cell type and
209 time point (Fig. 1 j-l, Extended Data Fig. 1c-e, 2a-b). In LPLC2 neurons at 48h APF,
210 the first principal component (PC1) captured a significant group of genes that were
211 expressed in a graded manner across individual neurons (Fig. 1j). For example,
212 the most differentially expressed gene across LPLC2 was dpr13. It displayed the
213 highest magnitude of within-cell-type variation of expression, but there was no
214 clear boundary separating neurons with high versus low dpr13 expression levels.
215 Many of the most differentially expressed genes were cell recognition molecules:
216 members of the Immunoglobulin Superfamily (IgSF) (e.g., dpr13, tei, beat-VI),
217 Leucine-rich-repeat (e.g., trn) and Cadherin (e.g., Cad87A) families[28,42](Fig, 1j).
218 We investigated whether this transcriptional heterogeneity reflected distinct
219 neuronal subtypes or a continuous variation, by forcing LPLC2 neurons to form
220 discrete clusters, and shuffling gene expression levels within and across clusters
221 (Extended Data Fig. 2c-g). Our analysis revealed that the heterogeneity was not
222 discrete, indicating that LPLC2 neurons form a continuum within a transcriptionally
223 similar neuronal type, rather than comprising several distinct subtypes. The
224 distribution of neurons along PC1 did not correlate with developmental age, sex,
225 genetic background, or mRNA coverage (Fig. 1k), indicating that the observed
226 within-cell-type continuous molecular heterogeneity had a different origin. The
227 graded expression of top differentially expressed genes associated with PC1 at
228 48h APF (including IgSF molecules dpr13, beat-VI, and tei, as well as SiaT

229 (Sialyltransferase)) was persistent throughout development and was also captured
230 by PC1 at 72h and 96h APF (Fig. 1l).
231 In LPLC1 neurons, PC1 also captured gradients of IgSF recognition
232 molecules (e.g., DIP-kappa, CG33543, dpr3, sdk) that were persistent throughout
233 development (Extended Data Fig. 1c-d). Similarly to LPLC2, molecular gradients
234 in LPLC1 could not be explained by differences in age, sex, genetic background,
235 or mRNA coverage across individual neurons (Extended Data Fig. 1e, 2a-b). In
236 contrast, molecular heterogeneity in LC4 neurons did not appear biologically
237 relevant. PC1 in LC4 correlated with the technical quality of single-cell
238 transcriptomes (number of transcripts captured per each neuron, Extended Data
239 Fig. 1e, 2a-b).
240 In summary, our analysis uncovered persistent expression gradients of
241 recognition molecules within LPLC1 and LPLC2 neurons. The absence of such
242 gradients in LC4 neurons suggests that molecular heterogeneity within cell types
243 may be a feature exclusive to VPNs lacking axonal retinotopy.
244

245 Spatial Transcriptomics Validates Molecular Gradients

246 We sought to independently verify within-cell-type gene expression
247 gradients in LPLC2. To do this, we used Single-Molecule Hairpin Chain Reaction
248 Fluorescent in Situ Hybridization[43] (HCR-FISH), a spatial transcriptomics method
249 that allows for the quantification of gene expression in individual cells. Combined
250 with Expansion-Assisted Light Sheet Microscopy[44], this approach enabled us to
251 visualize and count individual transcripts within neuronal somas (Fig. 2a). We
252 observed that individual LPLC2 somas, often positioned adjacent to one another,
253 exhibited striking differences in the numbers of mRNA transcripts for dpr13 and
254 SiaT, two of the most differentially expressed genes in the LPLC2 dataset (Fig. 2b-
255 c). Similar patterns were observed for beat-VI and dpr17, two differentially
256 expressed IgSF recognition molecules (Extended Data Fig. 3a-b).
257 To broaden our analysis to other genes, we tested pairs of genes that
258 exhibited correlated or anticorrelated expression patterns based on scRNA-seq
259 data (Fig. 1j) to determine if these relationships were replicated using HCR-FISH.
260 We quantified differential gene expression using Flyseg[45], an automated
261 volumetric instance segmentation algorithm we previously developed (see
262 Methods). The results of scRNA-seq and HCR-FISH were similar for genes
263 exhibiting antiparallel (e.g., dpr13 and SiaT, Fig. 2d, top) and parallel expression
264 patterns (e.g., dpr13 and beat-VI, Fig. 2d, bottom). Most of these relationships
265 remained consistent throughout development (Fig. 2e, Supplemental Table 2),
266 supporting our findings from scRNA-seq data. One exception was mbl
267 (*muscleblind*): although this gene exhibited graded expression in scRNA-seq (Fig.
268 1j), it showed low, uniform expression in HCR-FISH. The reason for this
269 discrepancy is unclear. Together, these data confirmed the presence of gene
270 expression gradients within the LPLC2 population.
271

272 Molecular Gradients Align with Synaptic Gradients

273 The cell bodies of the LPLC2 neurons where we measured different levels
274 of transcripts were arranged in salt-and-pepper fashion (Fig. 2c). LPLC2 dendrites

are, however, retinotopically arranged. We next investigated whether there was a correlation between the retinotopic position of LPLC2 dendrites and the expression level of genes. To do this, we used a genetic intersection method to selectively visualize neurons within a specific cell type that express a particular gene at a given time point (Fig. 2f-g). Recognition molecules dpr13, beat-VI, and Cad87A, which displayed correlated expression profiles in the scRNA-seq data (Fig. 1j), were predominantly expressed by LPLC2 neurons with dendrites in the dorsal region of the lobula at 48h APF (Fig. 2h-i, Extended Data Fig. 4a-b). Conversely, the expression of SiaT, dpr17, CG03419, Tsp42Ef, and stacl was limited to the ventral region at the same developmental stage (Fig. 2h-i, Extended Data Fig. 4c-d). We validated this DV heterogeneity using HCR-FISH, confirming that sparsely labeled dorsal LPLC2 contained significantly more dpr13 and beat-VI transcripts than their ventral counterparts (Extended Data Fig. 3c-d). Heterogeneous expression of recognition molecules DIP-kappa, dpr17 and sdk in LPLC1 neurons had similar retinotopic correlates (Extended Data Fig. 4e-f), suggesting that such retinotopically biased expression gradients are a general feature of many VPN cell types.

In summary, we found that the dendrites of individual neurons within a single VPN cell type, sampling different regions of the visual space, are molecularly heterogeneous. Across a VPN population, the neurons express gradients of recognition molecules that match the orientation of synaptic gradients in these VPNs. This observation suggests that even though the axons of these neurons are spatially intermingled, they maintain their molecular differences. Our next objective was to determine if these molecular and synaptic gradients have functional correlates.

The Dpr13::DIP-ε gradient forms a looming escape synaptic gradient

Above we showed that LPLC2 neurons express IgSF recognition molecules in a DV gradient, with dpr13 and beat-VI having higher expression levels in dorsal LPLC2 neurons, and dpr17 higher expression in ventral ones. We hypothesized that this DV gradient could provide the developmental origins for the gradient in synapse number between LPLC2 neurons and the GF observed in adult flies (Extended Data Fig. 5a). For this to be true, the GF would need to express cell surface proteins that bind one or more of the three recognition molecules we identified. This would allow the differential molecular expression in LPLC2 neurons to be converted into differential cell adhesion between individual LPLC2 neurons and the GF. Interaction maps for the IgSF molecules have previously been established and include interactomes of Dpr and DIP proteins (DIP/Dpr[42,46]), as well as interactomes of Beat and Side proteins (Beat/Side[47]; Fig. 3a). To test our hypothesis, we assessed expression levels of IgSF binding partners in the GF using HCR-FISH. DIP-ε, a binding partner of Dpr13, was the only gene showing strong expression in the GF during development (Fig. 3b-c).

To determine if DIP-ε played a role in forming connections between LPLC2 axons and GF dendrites, we next looked at the interaction between LPLC2 axons and GF dendrites in DIP-ε-deficient transgenic flies during development. In animals

321 with no DIP-ε (*DIP-ε^{null}* allele), we observed a ~10-fold decrease in axo-dendritic
322 overlap volume between LPLC2 axons and GF dendrites (Fig. 3d-e). Wild type
323 levels of axo-dendritic overlap could be restored in these *DIP-ε^{null}* flies by
324 overexpression of DIP-ε in just the GF in *DIP-ε^{null}* flies (Fig. 3f, Extended Data Fig.
325 5d). Knockdown of DIP-ε specifically in the GF using two different RNAi lines also
326 significantly reduced LPLC2-GF axo-dendritic overlap (Fig. 3f, Extended Data Fig.
327 5c). Thus, DIP-ε is required in the GF to establish connectivity with LPLC2 axons.
328 If DIP-ε is required to form functional LPLC2-GF synapses, then we would
329 expect that, compared to controls, DIP-ε-deficient flies shown looming stimuli
330 would have decreased GF responses and exhibit fewer GF-driven "short-mode"
331 takeoffs. Furthermore, we anticipate that, if too few LPLC2-GF synapses form to
332 make a DV gradient, then the number of short-mode takeoffs would no longer
333 increase with increasing elevation of the looming stimulus. To check these
334 hypotheses, we first performed whole-cell patch-clamp recordings in the GF while
335 presenting looming stimuli. As predicted, we observed a reduction in the peak
336 magnitude of the GF response in *DIP-ε^{null}* animals and in those expressing DIP-ε
337 RNAi in the GF compared to controls (Fig. 3h-i; Extended Data Fig. 6). We next
338 tested DIP-ε-deficient flies in our FlyPEZ behavior apparatus and found that both
339 *DIP-ε^{null}* animals and animals expressing DIP-ε RNAi in the GF displayed a
340 dramatic reduction in short-mode takeoff percentage at all stimulus elevations, and
341 a reduced difference between 0° and 77° elevations compared to the wild-type
342 control, indicative of reducing the functional synaptic gradient (Fig. 3j-k, Extended
343 Data Fig. 7a-b). Together with our anatomical findings, these functional data
344 further support a role for GF-expressed DIP-ε in establishing graded synaptic
345 connectivity with LPLC2.
346 We next sought to test the causal role of the dpr13::DIP-ε-defined gradient
347 on takeoff behavior by retaining strong LPLC2-GF connectivity but eliminating the
348 connectivity gradient. To achieve this, we increased the level of dpr13 uniformly
349 across the LPLC2 population (heretofore referred to as "overexpression").
350 Compared to controls, animals overexpressing dpr13 in LPLC2 exhibited a higher
351 percentage of short-mode takeoffs mediated by the GF (Fig. 3l, Extended Data
352 Fig. 7c). This gain-of-function was most pronounced at lower (0°) elevations,
353 decreased at 45°, and was absent at higher (77°) stimulus elevations, resulting in
354 no significant change in short-mode escape frequency with elevation. Thus, when
355 dpr13 is uniformly expressed across LPLC2 neurons, we observe an elimination
356 of the DV gradient of short-mode takeoffs that is seen in control animals (Fig. 3l).
357 Overexpression of dpr13 also led to an increase in LPLC2-GF axo-dendritic
358 overlap (Fig. 3m, Extended Data Fig. 5e-f). These data support a causal
359 relationship between the level of dpr13 and the number and graded distribution of
360 LPLC2 synapses onto the GF.
361 We next sought to examine the consequences of removing dpr13 on the
362 LPLC2-GF interaction. We examined LPLC2-GF axo-dendritic overlap in dpr13
363 null mutant (*dpr13^{null}* allele) animals (Extended Data Fig. 5g-h) and found no
364 difference from control animals. Our scRNA-seq data had revealed that LPLC2
365 neurons also express four other DIP-ε-interacting dprs (dpr14, dpr18, dpr19, and
366 dpr20; Extended Data Fig. 5i-j), suggesting there is indeed some functional

redundancy among the dprs expressed in LPLC2. However, unlike dpr13, the expression of these other dprs is not graded (Extended Data Fig. 5k). To address this, we ectopically expressed DIP-ε in LPLC2 with the intent of promoting *cis*-interactions between DIP-ε and all five Dpr paralogs, thereby inhibiting their *trans*-interactions with DIP-ε in the GF (an effect observed for other DIP/Dpr pairs[47,48]). This genetic manipulation reduced LPLC2-GF axo-dendritic overlap (Fig. 3n, Extended Data Fig. 5l-m), mimicking the phenotype of DIP-ε removal from the GF. Together, these findings indicate that multiple Dprs binding to DIP-ε collectively promote synaptic connectivity between LPLC2 axon terminals and GF dendrites in a redundant manner, while dpr13 specifically contributes to establishing the connectivity gradient.

In summary, DIP-ε and Dpr13 act as a ligand-receptor pair to control synaptic connectivity between LPLC2 and the GF. Our data supports a model in which a DV gradient of Dpr13::DIP-ε interactions, shaped by graded expression of dpr13 across LPLC2 neurons, specifies the formation of the DV gradient of synaptic weights (Extended Data Fig. 5l).

Beat-VI::Side-II gradient forms a motion detection synaptic gradient

We next investigated the functional role of other genes that displayed gradients of expression across LPLC2 neurons (Fig. 1h). Like dpr13, beat-VI, another IgSF recognition molecule[47], was also expressed in a DV gradient in LPLC2 (higher expression in dorsal, and lower in ventral LPLC2 – Fig. 2i, Extended Data Fig. 8a). However, neither the loss of beat-VI nor its binding partner side-II[46] affected the overlap between LPLC2 axon terminals and the GF dendrites (Extended Data Fig. 8b-c). This prompted us to investigate whether the beat-VI gradient might function in a different neuronal compartment by regulating graded inputs to LPLC2 dendrites instead.

We previously showed that beat-VI regulates synaptic specificity in the *Drosophila* motion detection circuit[50]; beat-VI and its interacting partner side-II[47] are required for matching motion-detecting T4d/T5d neurons with their postsynaptic partners in layer 4 of the lobula plate (LoP4), which encodes downward motion. Because LPLC2 is a part of this circuit, receiving excitatory inputs from T4/T5 neurons in all four LoP layers[6] (Fig. 4a, top), we hypothesized that the beat-VI gradient might similarly influence LPLC2 dendritic connectivity.

Each LPLC2 neuron has four dendritic branches in the lobula plate, one in each layer, extending in four cardinal directions, corresponding to motion sensitivity in each layer[6] (Fig. 4a, bottom). The response at the LPLC2 axon is a non-linear sum of the activity in each of these four branches. Individual LPLC2 neurons thus serve as “looming detectors”. They respond most strongly to looming stimuli that originate at their receptive field center extending radially outward simultaneously generating motion in all four cardinal directions, thereby maximally exciting each of the four dendritic branches[6]. Using “FAFB-Flywire”[32,33] connectome reconstruction, we found that two of the four classes of T4/T5 neurons, T4c/T5c and T4d/T5d, form antiparallel DV synaptic gradients onto LPLC2 dendrites in Lop3 and Lop4, respectively (Fig. 4b).

These findings suggest that dorsal and ventral LPLC2 neurons within one animal may receive differential amounts of upward and downward motion information, potentially linked to the molecular gradient of beat-VI. Supporting this idea, RNAi knockdown of beat-VI differentially affected LPLC2 dendrites depending on their retinotopic location. LoP4 branches were missing in dorsal LPLC2, while central LPLC2 exhibited a milder phenotype, and ventral LPLC2 were unaffected (Fig. 4c-d – single cell sparse visualization, Extended Data Fig. 8d-e – whole population labeling). Similarly, removing side-II from T4/T5 neurons produced a graded phenotype, while overexpression of beat-VI in LPLC2 caused abnormal LoP4 dendritic branching in dorsal, but not ventral, LPLC2 neurons (Fig. 4e, Extended Data Fig. 8f-g). These results support the idea that DV-graded variations in Beat-VI and Side-II interactions differentially regulate the connectivity between T4d/T5d axons and LPLC2 dendrites.

To determine whether beat-VI deficiency in LPLC2 had functional effects, we performed a directional tuning experiment combined with calcium imaging in individual LPLC2 neurons. We imaged from the unbranched neurite that connects an LPLC2 neuron's dendrites in the LoP and Lo (see Methods, Fig. 4f-h, Extended Data Fig 9), which has previously been shown to have weak responses to a small bar moving in each of four cardinal directions (i.e., stimuli exciting LPLC2 dendrite branches in a single LoP layer) and a much larger response to looming (i.e., stimuli exciting LPLC2 dendritic branches in all four LoP layers simultaneously)[6].

Our results showed that wild type dorsal and ventral LPLC2 neurons exhibited different patterns of responses to directional stimuli. Ventral LPLC2 showed little to no response to downward motion, as would be expected if they received little input from downward sensing T4d/T5d neurons in LoP layer 4 (Fig. 4i, bottom, Extended Data Fig. 9b-e). As a result, responses to stimuli presented in all directions showed a bias towards upward motion (Fig. 4j). In contrast, dorsal LPLC2 neurons were more omnidirectional, as expected if synaptic inputs from all four LoP layers was more evenly balanced (Fig 4i-j, Extended Data Fig. 9b-e). Notably, after beat-VI knockdown, dorsal LPLC2 neuron responses became biased for upward motion, similar to their wild-type ventral counterparts, consistent with down selective T4d/T5d input being reduced. Beat-VI knockdown had little effect on ventral LPLC2 neurons, which remained biased for upward motion (Fig. 4j, Extended Data Fig. 9b-c, e). A heatmap summarizing the experimental effects showed that beat-VI knockdown disrupted the normal directional tuning biases of LPLC2 neurons (Fig. 4k) without significantly affecting their responses to looming stimuli (Fig. 4l, Extended Data Fig. 9f).

Together, these findings suggest that Beat-VI and Side-II act as a ligand-receptor pair to control synaptic connectivity between T4d/T5d and LPLC2 neurons. Our data support a model in which the DV gradient of Beat-VI::Side-II interactions contributes to the formation of the DV gradient of synaptic weights between T4d/T5d and LPLC2 neurons, decreasing the response to downward motion by LPLC2 neurons with ventral receptive fields.

Discussion

In this study, we identified the molecular origins of two parallel dorsoventral synaptic gradients in the axons and dendrites of LPLC2, the looming-detecting VPN cell type. These synaptic gradients translate retinotopic information from the fly's visual field into specific motor outputs. We demonstrate that a gradient of Beat-VI::Side-II IgSF recognition proteins regulates the graded synaptic inputs from T4d/T5d neurons onto LPLC2, sculpting differential integration of the downward motion component in the looming stimulus across different regions of the eye. Similarly, a gradient of DIP-ε::Dpr13, another pair of IgSF recognition molecules, shapes the graded synaptic outputs of LPLC2 onto the Giant Fiber, biasing escape towards faster takeoffs in response to looming stimuli from the dorsal visual field. These synaptic gradients, however, are distinct from each other. For the dendritic synaptic gradient, there is a retinotopic match between populations of input neurons (T4d/T5d) and the postsynaptic LPLC2 neurons (i.e., *many-to-many with retinotopy*). By contrast, multiple LPLC2 axons form different numbers of synapses onto the dendrites of a single cell (GF) (i.e., *many-to-one* without retinotopy). Irrespective of these differences, our findings suggest a molecular model of synaptic specificity, in which the expression levels of recognition molecules establish synapse numbers.

What is the relationship between the parallel gradients of beat-VI and dpr13 expression and the number of synaptic inputs to and outputs from LPLC2? In a beat-VI loss-of-function experiment, the severity of functional consequences was directly proportional to beat-VI expression levels in individual LPLC2 neurons. The morphological phenotypes were similar whether beat-VI was removed from LPLC2 or side-II from T4/T5 neurons, with the reduction in LoP4 dendritic branching also corresponding to beat-VI expression levels. However, it remains unclear whether this phenotype arises from a failure to extend dendrites, or to stabilize them. We propose that beat-VI and side-II promote adhesion between T4d/T5d axons and LPLC2 dendrites, with the strength of this adhesion correlating with beat-VI expression levels. This protein interaction could influence synapse number either indirectly, by increasing the area of contact between T4d/T5d axons and LPLC2 dendrites, or directly, by controlling synapse formation, with decreased synapse numbers leading to reduced axo-dendritic contact.

Dpr13 and DIP-ε are essential for establishing synaptic connections between LPLC2 neurons and the GF. Loss of DIP-ε function reduced the overlap between LPLC2 axons and the GF dendrites, leading to significant defects in GF responses to looming stimuli, as demonstrated by both behavioral and electrophysiological assays. Analyzing the loss of dpr13 function is complicated by the presence of four additional Dpr paralogs in LPLC2, interacting with DIP-ε with similar binding affinities. By ectopically expressing DIP-ε in LPLC2, we inhibited all DIP-ε-interacting Dprs in LPLC2. This phenocopied the DIP-ε loss-of-function phenotype in the GF, providing additional support for the interactions between DIP-ε in the GF dendrites with its cognate binding Dprs in LPLC2 axons. The role of multiple Dpr paralogs interacting with DIP-ε may be to ensure baseline synaptic connectivity in the crucial escape circuit, while the formation of the synaptic gradient depends specifically on dpr13. In support of this, increasing dpr13

expression uniformly across the LPLC2 population eliminated the graded behavioral response to dorsal versus ventral looming stimuli, along with increasing the LPLC2-GF axo-dendritic overlap. These observations support the idea that Dpr13::DIP-ε interactions control the number of synapses formed between two neurons, resulting in the formation of a synaptic gradient between LPLC2 and the GF. However, the precise mechanism by which this occurs remains unclear. Future studies should investigate the development of these synapses in detail, to assess the consequences of changing dpr13 levels in individual neurons using mosaic animals, and employing EM reconstruction or expansion microscopy to elucidate how dpr13 and DIP-ε contribute to synaptic gradient formation at a mechanistic level.

The dpr13::DIP-ε gradient functions differently from Eph and Ephrin gradients in vertebrate retinotectal maps[51,52]. Both gradients relay visual-spatial information from the eye to the brain but use distinct strategies. Ephrins and Ephs form topographic maps by maintaining the positional information of neurons in the retina to arrangement of their axons in the midbrain[53] (i.e., retinotopy). In contrast, the dpr13::DIP-ε gradient translates positional information from VPN dendrites into synapse numbers in the central brain, independent of axon retinotopy. This represents a new molecular mechanism of visuomotor transformation.

As most VPNs form synaptic gradients[5], varying levels of adhesion molecules may represent a general strategy for regulating synapse numbers. Notably, altering levels of SynCAM1, another IgSF adhesion molecule, also affects synapse numbers in the mammalian hippocampus[54]. Together, these data suggest that not only do the cell recognition molecules determine synaptic specificity by qualitatively matching synaptic partners[26–28] (a classic notion established through decades of genetic studies), but that their expression levels may also influence the number of synapses formed between matched neurons with functional and behavioral consequences. This variation holds an enormous potential for fine-tuning ethologically relevant behavioral responses driven by complex neural circuits.

Our work has uncovered graded molecular heterogeneity within single VPN cell types. This feature is distinct from discrete[38,41] or stochastic[55,56] variations in gene expression within neuronal types previously described in *Drosophila*. We identified many graded genes in VPNs beyond cell recognition molecules, suggesting that molecular gradients may regulate other cellular and circuit functions. These findings are particularly interesting as cell types in the mammalian cortex also exhibit continuous transcriptomic variation[8,57–59]. These data raise the possibility that within-cell-type molecular heterogeneity could be a common mechanism for generating neuronal diversity which, in turn, contribute to synaptic specificity.

In conclusion, we describe a new molecular strategy regulating neural circuit assembly. This was enabled through detailed EM-connectomics of the fly brain[22,31,33] and rapid advances in single-cell sequencing technologies. We anticipate that merging these approaches to study the mammalian brain[60,61] will uncover new molecular mechanisms underlying wiring specificity.

References

1. Shin, S., Crapse, T. B., Angeles, L., Mayo, J. P. & Sommer, M. A. Visuomotor Integration. *Encycl. Neurosci.* (2009).
2. Andersen, R. A., Snyder, L. H., Li, C. S. & Stricanne, B. Coordinate transformations in the representation of spatial information. *Curr. Opin. Neurobiol.* **3**, 171–176 (1993).
3. Otsuna, H. & Ito, K. Systematic analysis of the visual projection neurons of Drosophila melanogaster. I. Lobula-specific pathways. *J. Comp. Neurol.* **497**, 928–958 (2006).
4. Wu, M. *et al.* Visual projection neurons in the Drosophila lobula link feature detection to distinct behavioral programs. *Elife* **5**, 1–43 (2016).
5. Dombrovski, M. *et al.* Synaptic gradients transform object location to action. *Nature* **613**, 534–542 (2023).
6. Klapoetke, N. C. *et al.* Ultra-selective looming detection from radial motion opponency. *Nature* **551**, 237–241 (2017).
7. Von Reyn, C. R. *et al.* A spike-timing mechanism for action selection. *Nat. Neurosci.* **17**, 962–970 (2014).
8. Cembrowski, M. S. & Menon, V. Continuous Variation within Cell Types of the Nervous System. *Trends Neurosci.* **41**, 337–348 (2018).
9. Ghahramani, Z., Wolpert, D. M. & Jordan, M. I. Generalization to local remappings of the visuomotor coordinate transformation. *J. Neurosci.* **16**, 7085–7096 (1996).
10. Fujiwara, Y., Lee, J., Ishikawa, T., Kakei, S. & Izawa, J. Diverse coordinate frames on sensorimotor areas in visuomotor transformation. *Sci. Reports 2017 71* **7**, 1–9 (2017).
11. Buneo, C. A., Jarvis, M. R., Batista, A. P. & Andersen, R. A. Direct visuomotor transformations for reaching. *Nature* **416**, 632–636 (2002).
12. Helmbrecht, T. O., dal Maschio, M., Donovan, J. C., Koutsouli, S. & Baier, H. Topography of a Visuomotor Transformation. *Neuron* **100**, 1429-1445.e4 (2018).
13. Kim, J. H., Ma, D. H., Jung, E., Choi, I. & Lee, S. H. Gated feedforward inhibition in the frontal cortex releases goal-directed action. *Nat. Neurosci. 2021 2410* **24**, 1452–1464 (2021).
14. Huston, S. J. & Jayaraman, V. Studying sensorimotor integration in insects. *Curr. Opin. Neurobiol.* **21**, 527–534 (2011).
15. Cruz, T. L. & Chiappe, M. E. Multilevel visuomotor control of locomotion in Drosophila. *Curr. Opin. Neurobiol.* **82**, 102774 (2023).
16. Wang, T. S. L., Martinez, M., Festa, E. K., Heindel, W. C. & Song, J. H. Age-related enhancement in visuomotor learning by a dual-task. *Sci. Reports 2022 121* **12**, 1–12 (2022).
17. Dombrovski, M. *et al.* A Plastic Visual Pathway Regulates Cooperative Behavior in Drosophila Larvae. *Curr. Biol.* (2019) doi:10.1016/j.cub.2019.04.060.
18. Zada, D. *et al.* Development of neural circuits for social motion perception in schooling fish. *Curr. Biol.* **0**, (2024).
19. Wei, P. *et al.* Processing of visually evoked innate fear by a non-canonical

596 thalamic pathway. *Nat. Commun. 2015 61* **6**, 1–13 (2015).
597 20. Zhao, P. *et al.* The visuomotor transformations underlying defensive
598 behaviors and hunting. *bioRxiv* 2024.05.07.592863 (2024)
599 doi:10.1101/2024.05.07.592863.
600 21. Cande, J. *et al.* Optogenetic dissection of descending behavioral control in
601 Drosophila. *Elife* **7**, (2018).
602 22. Nern, A. *et al.* Connectome-driven neural inventory of a complete visual
603 system. *bioRxiv* 2024.04.16.589741 (2024)
604 doi:10.1101/2024.04.16.589741.
605 23. Klapoetke, N. C. *et al.* A functionally ordered visual feature map in the
606 Drosophila brain. *Neuron* **110**, 1700-1711.e6 (2022).
607 24. Aptekar, J. W., Keleş, M. F., Lu, P. M., Zolotova, N. M. & Frye, M. A.
608 Neurons forming optic glomeruli compute figure–ground discriminations in
609 Drosophila. *J. Neurosci.* **35**, 7587–7599 (2015).
610 25. Keleş, M. F. & Frye, M. A. Object-Detecting Neurons in Drosophila. *Curr.*
611 *Biol.* **27**, 680–687 (2017).
612 26. Margeta, M. A. & Shen, K. Molecular mechanisms of synaptic specificity.
613 *Mol. Cell. Neurosci.* **43**, 261–267 (2010).
614 27. Südhof, T. C. Towards an Understanding of Synapse Formation. *Neuron*
615 **100**, 276 (2018).
616 28. Sanes, J. R. & Zipursky, S. L. Synaptic Specificity, Recognition Molecules,
617 and Assembly of Neural Circuits. *Cell* **181**, 536–556 (2020).
618 29. Bacon, J. P. & Strausfeld, N. J. The dipteran 'Giant fibre' pathway: neurons
619 and signals. *J. Comp. Physiol. A* **158**, 529–548 (1986).
620 30. Jang, H., Goodman, D. P., Ausborn, J. & von Reyn, C. R. Azimuthal
621 invariance to looming stimuli in the Drosophila giant fiber escape circuit. *J.*
622 *Exp. Biol.* **226**, (2023).
623 31. Scheffer, L. K. *et al.* A connectome and analysis of the adult drosophila
624 central brain. *Elife* **9**, 1–74 (2020).
625 32. Zheng, Z. *et al.* A Complete Electron Microscopy Volume of the Brain of
626 Adult Drosophila melanogaster. *Cell* **174**, 730-743.e22 (2018).
627 33. Schlegel, P. *et al.* Whole-brain annotation and multi-connectome cell typing
628 quantifies circuit stereotypy in Drosophila. *bioRxiv* 2023.06.27.546055
629 (2023) doi:10.1101/2023.06.27.546055.
630 34. Card, G. & Dickinson, M. H. Visually Mediated Motor Planning in the
631 Escape Response of Drosophila. *Curr. Biol.* **18**, 1300–1307 (2008).
632 35. Williamson, R., Peek, M. Y., Breads, P., Coop, B. & Card, G. M. Tools for
633 Rapid High-Resolution Behavioral Phenotyping of Automatically Isolated
634 Drosophila. *Cell Rep.* **25**, (2018).
635 36. Ache, J. M. *et al.* Neural Basis for Looming Size and Velocity Encoding in
636 the Drosophila Giant Fiber Escape Pathway. *Curr. Biol.* **29**, 1073-1081.e4
637 (2019).
638 37. Moreno-Sanchez, A. *et al.* Morphology and synapse topography optimize
639 linear encoding of synapse numbers in Drosophila looming responsive
640 descending neurons. *bioRxiv Prepr. Serv. Biol.* (2024)
641 doi:10.1101/2024.04.24.591016.

642 38. Kurmangaliyev, Y. Z., Yoo, J., Valdes-Aleman, J., Sanfilippo, P. &
643 Zipursky, S. L. Transcriptional Programs of Circuit Assembly in the
644 Drosophila Visual System. *Neuron* **108**, 1045-1057.e6 (2020).
645 39. Kang, H. M. *et al.* Multiplexed droplet single-cell RNA-sequencing using
646 natural genetic variation. *Nat. Biotechnol. 2017 361* **36**, 89–94 (2017).
647 40. MacKay, T. F. C. *et al.* The Drosophila melanogaster Genetic Reference
648 Panel. *Nature* **482**, 173–178 (2012).
649 41. Özel, M. N. *et al.* Neuronal diversity and convergence in a visual system
650 developmental atlas. *Nature* **589**, 88–95 (2021).
651 42. Özkan, E. *et al.* An extracellular interactome of immunoglobulin and LRR
652 proteins reveals receptor-ligand networks. *Cell* **154**, 228 (2013).
653 43. Choi, H. M. T. *et al.* Third-generation in situ hybridization chain reaction:
654 multiplexed, quantitative, sensitive, versatile, robust. *Development* **145**,
655 (2018).
656 44. Lillvis, J. L. *et al.* Rapid reconstruction of neural circuits using tissue
657 expansion and light sheet microscopy. *Elife* **11**, 1–36 (2022).
658 45. Vaccari, A. & Dombrovski, M. FlySeg: An Automated Volumetric Instance
659 Segmentation Algorithm for Dense Cell Populations in Drosophila
660 Melanogaster Nervous System. *Conf. Rec. - Asilomar Conf. Signals, Syst.*
661 *Comput.* 1474–1478 (2023)
662 doi:10.1109/IEEECONF59524.2023.10476819.
663 46. Cosmanescu, F. *et al.* Neuron-Subtype-Specific Expression, Interaction
664 Affinities, and Specificity Determinants of DIP/Dpr Cell Recognition
665 Proteins. *Neuron* **100**, 1385-1400.e6 (2018).
666 47. Li, H. *et al.* Deconstruction of the beaten path-sidestep interaction network
667 provides insights into neuromuscular system development. *Elife* **6**, (2017).
668 48. Menon, K. P., Kulkarni, V., Shin-Ya, T., Anaya, M. & Zinn, K. Interactions
669 between dpr11 and dip-y control election of amacrine neurons in
670 drosophila color ision circuits. *Elife* **8**, 1–32 (2019).
671 49. Morano, N. C. *et al.* Cis inhibition of co-expressed DIPs and Dprs shapes
672 neural development. *bioRxiv* 2024.03.04.583391 (2024)
673 doi:10.1101/2024.03.04.583391.
674 50. Yoo, J. *et al.* Brain wiring determinants uncovered by integrating
675 connectomes and transcriptomes. *Curr. Biol.* **33**, 3998-4005.e6 (2023).
676 51. Brown, A. *et al.* Topographic mapping from the retina to the midbrain is
677 controlled by relative but not absolute levels of EphA receptor signaling.
678 *Cell* **102**, 77–88 (2000).
679 52. Triplett, J. W. & Feldheim, D. A. Eph and ephrin signaling in the formation
680 of topographic maps. *Semin. Cell Dev. Biol.* **23**, 7 (2012).
681 53. Kita, E. M., Scott, E. K. & Goodhill, G. J. Topographic wiring of the
682 retinotectal connection in zebrafish. *Dev. Neurobiol.* **75**, 542–556 (2015).
683 54. Robbins, E. M. *et al.* SynCAM 1 Adhesion Dynamically Regulates Synapse
684 Number and Impacts Plasticity and Learning. *Neuron* **68**, 894–906 (2010).
685 55. Wernet, M. F. *et al.* Stochastic spineless expression creates the retinal
686 mosaic for colour vision. *Nature* **440**, 174–180 (2006).
687 56. Miura, S. K., Martins, A., Zhang, K. X., Graveley, B. R. & Zipursky, S. L.

688 Probabilistic splicing of Dscam1 establishes identity at the level of single
689 neurons. *Cell* **155**, 1166 (2013).
690 57. Cembrowski, M. S. & Spruston, N. Heterogeneity within classical cell types
691 is the rule: lessons from hippocampal pyramidal neurons. *Nat. Rev.*
692 *Neurosci. 2019 204* **20**, 193–204 (2019).
693 58. Cheng, S. *et al.* Vision-dependent specification of cell types and function in
694 the developing cortex. *Cell* **185**, 311-327.e24 (2022).
695 59. Yao, Z. *et al.* A taxonomy of transcriptomic cell types across the isocortex
696 and hippocampal formation. *Cell* **184**, 3222-3241.e26 (2021).
697 60. Sievers, M. *et al.* Connectomic reconstruction of a cortical column. *bioRxiv*
698 2024.03.22.586254 (2024) doi:10.1101/2024.03.22.586254.
699 61. Yao, Z. *et al.* A high-resolution transcriptomic and spatial atlas of cell types
700 in the whole mouse brain. *Nature* **624**, 317–332 (2023).
701 62. Gramates, L. S. *et al.* FlyBase: a guided tour of highlighted features.
702 *Genetics* **220**, (2022).
703 63. Kang, H. M. *et al.* Multiplexed droplet single-cell RNA-sequencing using
704 natural genetic variation. *Nat. Biotechnol. 2017 361* **36**, 89–94 (2017).
705 64. Li, H. A statistical framework for SNP calling, mutation discovery,
706 association mapping and population genetical parameter estimation from
707 sequencing data. *Bioinformatics* **27**, 2987–2993 (2011).
708 65. Hao, Y. *et al.* Dictionary learning for integrative, multimodal and scalable
709 single-cell analysis. *Nat. Biotechnol.* **42**, 293–304 (2024).
710 66. Gabbiani, F., Krapp, H. G. & Laurent, G. Computation of Object Approach
711 by a Wide-Field, Motion-Sensitive Neuron. *J. Neurosci.* **19**, 1122–1141
712 (1999).
713 67. Frighetto, G. & Frye, M. A. Columnar neurons support saccadic bar
714 tracking in Drosophila. *Elife* **12**, (2023).
715 68. Reiser, M. B. & Dickinson, M. H. A modular display system for insect
716 behavioral neuroscience. *J. Neurosci. Methods* **167**, 127–139 (2008).
717 69. Zhao, A. *et al.* Eye structure shapes neuron function in Drosophila motion
718 vision. *bioRxiv* 2022.12.14.520178 (2022) doi:10.1101/2022.12.14.520178.
719 70. DeBruine, L. M. & Barr, D. J. Understanding Mixed-Effects Models Through
720 Data Simulation. *Adv. Methods Pract. Psychol. Sci.* **4**, (2021).
721 71. Saravanan, V., Berman, G. J. & Sober, S. J. Application of the hierarchical
722 bootstrap to multi-level data in neuroscience. *Neurons, Behav. data Anal.*
723 *theory* **3**, (2020).
724 72. Xu, S. *et al.* Interactions between the Ig-Superfamily Proteins DIP-α and
725 Dpr6/10 Regulate Assembly of Neural Circuits. *Neuron* **100**, 1369-1384.e6
726 (2018).
727 73. Xu, H. *et al.* Sequence determinants of improved CRISPR sgRNA design.
728 *Genome Res.* **25**, 1147–1157 (2015).
729 74. Ren, X. *et al.* Optimized gene editing technology for Drosophila
730 melanogaster using germ line-specific Cas9. *Proc. Natl. Acad. Sci. U. S. A.*
731 **110**, 19012–19017 (2013).
732 75. Wassie, A. T., Zhao, Y. & Boyden, E. S. Expansion microscopy: principles
733 and uses in biological research. *Nat. Methods* **16**, 33–41 (2019).

76. Wang, Y. *et al.* EASI-FISH for thick tissue defines lateral hypothalamus spatio-molecular organization. *Cell* **184**, 6361-6377.e24 (2021).
77. Lee, P. T. *et al.* A gene-specific T2A-GAL4 library for Drosophila. *Elife* **7**, (2018).
78. Nern, A., Pfeiffer, B. D. & Rubin, G. M. Optimized tools for multicolor stochastic labeling reveal diverse stereotyped cell arrangements in the fly visual system. *Proc. Natl. Acad. Sci. U. S. A.* **112**, E2967–E2976 (2015).
79. Matsliah, A. *et al.* Neuronal "parts list" and wiring diagram for a visual system. *bioRxiv* (2024) doi:10.1101/2023.10.12.562119.

Materials and Methods

Experimental model details

Flies were reared under standard conditions at 25 °C and 50% humidity with a 12-h light/12-h dark cycle on a standard cornmeal fly food. Males and females 1-3 days after eclosion were used for all experiments except where specified. Supplementary Table 1 provides detailed descriptions of fly genotypes used in each experiment and origins of transgenic stocks. For developmental experiments, white pre-pupae (0h APF) were collected and incubated at 25 °C for the indicated number of hours.

scRNA-seq experiment

Virgin females carrying LPLC2, LPLC1 or LC4 split-GAL4 driver lines were crossed to males expressing a nuclear GFP reporter (UAS-His2A-GFP) and carrying unique 3rd chromosomes from the isogenic wild-type strains with known genotypes (DGRP, *Drosophila* Reference Genetic Panel[40]). Each experimental condition (cell type and time point) was crossed to 6 unique DGRP strains (see Supplemental Table 1 and Source Data for details; LC4 driver was crossed into 4 DGRP strains for 72 and 96h APF time points). Each of these crosses was considered an independent biological replicate. F1 generation animals (males and females) were collected at 0h APF and incubated for either 48h, 72h or 96 hours at 25°C. To introduce a control for developmental age, we split 6 DGRPs (for each cell type and time point) into equal "early" and "late" groups (Fig. 1g, see Source data for a detailed breakdown). Animals from "early" DGRPs were continuously staged and collected within the 2h time window, after which we continuously staged and collected animals from "late" DGRPs within the next 2h time window. This ensured that by the time brains were dissected (after 48, 72 or 96 hours), animals from the "early" group were on average 2h older than their "late" counterparts. Brains were dissected in ice-cold Schneider's *Drosophila* Medium (GIBCO #21720-024), collected in three Eppendorf tubes (each time point was processed as a separate sample) and kept on ice. Brains were incubated in mix of papain (Worthington #LK003178, 1000 units/ml) and Liberase™ (Sigma-Aldrich #5401119001, 0.18 Wu/ml) at 25°C for 30 min shaking at 1000rpm, washed twice

779 with 2% Bovine Serum Albumin (BSA, Sigma #B6917) in Schneider's Medium,
780 followed by two washes in 1% BSA in PBS. Finally, brains were transferred to
781 0.04% BSA in PBS and dissociated mechanically by pipetting. The cell suspension
782 was filtered through a 20 µm cell-strainer (Corning #352235) and sorted by FACS
783 (BD FACS Aria II) to purify GFP+ cells. Single-cell suspensions were used to
784 generate scRNA-seq libraries using the 10X Genomics Chromium Next GEM
785 Single Cell 3'-kit (v3.1) following the manufacturer's protocol. Each sample
786 (corresponding to a single time point) was loaded to a single lane of 10X
787 Chromium. Three scRNA-seq libraries were sequenced using one lane of
788 NovaSeq 6000 SP platform (28bp + 91 bp). The library preparation and
789 sequencing were performed by the Technology Center for Genomics and
790 Bioinformatics at UCLA.
791

792 **scRNA-seq data processing and analysis**

793 Raw scRNA-Seq reads were processed using Cell Ranger (10X Genomics,
794 version: 7.1.0). The reference genome and gene annotations were downloaded
795 from FlyBase[62] (release 6.29). Each time point was processed separately. Six
796 biological replicates were tagged with a unique wild-type chromosome, and
797 demultiplexed based on a unique wild-type chromosome using demuxlet[63] (version
798 2, https://github.com/statgen/popscle). Demultiplexing was performed using
799 single-nucleotide polymorphisms (SNPs) from 7 DGRP strains used in
800 experiments (see supplemental table 1 for the full list of genotypes and Source
801 Data for the list of DGRP strains used for each genotype and time point) and 3
802 additional DGRP strains as negative controls (line_129, line_427, line 712). SNPs
803 were filtered using the following criteria: (1) only bi-allelic SNPs on the 3rd
804 chromosome without missing data (called in all 10 strains); (2) non-reference allele
805 only in 1 of 10 strains. We quantified allelic counts for filtered SNPs using samtools
806 mpileup[64] (version 1.10). SNPs with a minimum total coverage of 10 in all three
807 samples (time points) and a maximum non-reference allele frequency of 0.25 were
808 kept for downstream analysis (34,655 SNPs). Only a few cells (0.1-0.2%) were
809 erroneously assigned to negative controls; 5–15% of cells were classified as
810 "doublets" and "ambiguous" (mostly cells with low transcript coverage). We
811 removed cells with less than 10,000 or more than 50,000 transcripts per cell (and
812 more than 10% of mitochondrial transcripts). The final dataset included 2,595 cells
813 for 48h APF, 2,369 cells for 72h APF, and 1,039 cells for 96h APF.

814 The scRNA-seq analysis was performed using Seurat[65] package (5.0.1). The
815 analysis was performed separately for each time point using the standard Seurat
816 workflow: raw transcript counts were normalized, 1000 highly variable genes were
817 scaled and used for PCA, first 5 PCs were used for clustering (resolution: 0.05)
818 and to calculate t-SNE projections. We use t-SNE projection only for the summary
819 visualization of the dataset. Clusters were annotated based on known marker
820 genes[38] (Fig. 1h-i and Extended Data Fig. 1d). Most of the cells corresponded to
821 LPLC2, LPLC1, and LC4 neurons. To explore further heterogeneity within VPN
822 type, we subsetted each cell type at each time point, identified 500 highly variable
823 genes, and repeated PCA. We plotted known biological and technical covariates

824 along each analyzed PC (Fig. 1k and Extended Data Fig. 1-2), including
825 developmental age, DGRP genotype, sex, and coverage (i.e., transcripts per cell).
826 PC1s in LPLC2 and LPLC1 did not correlate with any of these covariates and were
827 driven by similar sets of genes (Fig. 1j, l and Extended Data Fig. 1e-f). Further *in*
828 *vivo* validations using orthogonal approaches confirmed that these PCs captured
829 true molecular heterogeneity within each of these cell types (Fig. 2).

830

831 ## Behavioral experiments

832 **High-throughput takeoff assay**

833 High-throughput takeoff assay was performed with the FlyPEZ system, which
834 allows for the near-automated collection of fly behaviors in response to visual
835 stimulation in large sample sizes. FlyPEZ experiments were performed as
836 previously described[35]. Briefly, untrained flies (3-5 days old, both males and
837 females) were individually dispensed onto a 5 mm by 5 mm glass recording
838 platform via an automated "FlyGate" module[35], which controls the opening and
839 closing of the gate using a laser light sheet and linear photodetector. Once the fly
840 reaches the platform, four mirrors allow simultaneous recording of two views of the
841 fly (a bottom view and a side view) onto a single camera lens, which enables real-
842 time detection of the center of mass and heading of the fly via the "FlyDetect"
843 algorithm. The heading direction is then used to generate looming stimulation in
844 fly coordinates, and the behavioral response of the fly is recorded by a high-speed
845 camera at 6,000 frames per second under infrared illumination. A single stimulus
846 was presented per fly. All behavioral experiments were performed 4 hours before
847 incubator lights were switched off, which coincides with the flies' activity peak in
848 the afternoon light cycle.

849

850 **Visual stimulation for behavioral assay**

851 A 7-inch-diameter back-projection coated dome is placed centered over the glass
852 platform to present visual stimulation. Specifically, dark looming disks that
853 approach the fly from azimuth of 0° (front looms) or 90° (side looms), at elevations
854 of -30°, 0°, 23°, 45°, or 77° in fly coordinates were used. Looming stimuli were
855 generated using the same equation as described for calcium imaging experiments
856 (see below). All looming stimuli have l/v=40ms. Experiments in Figure 1e and Ext.
857 Fig 1a show trials that were performed in the past (from 2014 to 2024) using control
858 flies. Both looming disks expanding from 10° to 180° and 5° to 90° were combined
859 to get enough trials. Experiments in Figure 3 include trials with looming disks
860 expanding from 10° to 180° only.

861

862 **Behavioral data analysis**

863 To quantify the duration of the takeoff sequence, videos were manually annotated
864 to identify the start of the sequence (the first frame of wing-rising) and the end of
865 the sequence (the last frame that shows T2 legs in contact with the platform).
866 Takeoff sequence durations between 0ms to 7ms were considered "short-mode
867 takeoffs," and takeoff sequence durations longer than 7ms were considered "long-
868 mode takeoffs," as described previously[7]. The total takeoff percentage is

869 calculated by the number of takeoffs divided by the total number of trials. Short-
870 mode takeoff percentage is calculated by the number of short-mode takeoffs
871 divided by the total number of takeoffs. For experiments in Figure 1d, 1e, and Ext.
872 Fig 1c, takeoff sequence duration longer than 50ms was eliminated as outliers. All
873 takeoff sequence durations were less than 50ms for experiments in Figure 3.
874
875 **Statistical analysis**
876 Statistical comparison of the percentages of short-mode takeoffs was performed
877 with the Chi-squared test, with post-hoc Bonferroni correction for multiple
878 comparisons. Statistical comparison of takeoff sequence distributions between two
879 samples was performed with the Mann-Whitney U test. Statistical comparison of
880 takeoff sequence distributions between more than two samples was performed
881 with the Kruskal-Wallis test, with post-hoc Dunn correction for multiple
882 comparisons. Analysis and plotting were conducted with custom scripts in
883 MATLAB 2022b, and Scipy and Seaborn in Python 3.
884
885 ## Electrophysiological experiments
886
887 **Electrophysiological recordings**
888 In vivo whole-cell, current-clamp electrophysiology was performed on behaving,
889 tethered flies as previously described[30]. Flies were anesthetized at 4°C and their
890 head and thorax were attached to polyether ether ketone plates with UV glue
891 (Loctite 3972). The T1 legs were severed at the femur to prevent cleaning of the
892 head and obstruction of the eyes. The proboscis was secured in its retracted
893 position to minimize brain movement during the recording. The antennae were also
894 fixed with UV glue to restrict stimulation of antennal afferents to the GF. To access
895 the GF for recordings, the cuticle and trachea on the posterior side of the head
896 above the GF soma were removed and the brain was perfused with standard
897 extracellular saline (NaCl 103 mmol, KCl 3 mmol, TES 5 mmol, trehalose-$2H_2O$ 8
898 mmol, glucose 10 mmol, $NaHCO_3$ 26 mmol, NaH_2PO_4 1 mmol, $CaCl_2 \cdot 2H_2O$ 1.5
899 mmol, and $MgCl_2 \cdot 6H_2O$ 4 mmol; Gouwens and Wilson 2009). Osmolarity was
900 adjusted to 270–275 mOsm and bubbled with 95% O2/5% CO2 to maintain a pH
901 of 7.3. All experiments were conducted at room temperature (20–22°C). A brief,
902 localized application of collagenase (0.5% in extracellular saline) with a glass
903 electrode was used to disrupt the brain sheath and access the soma for recording.
904 GFP-labeled soma was then targeted by patch-clamp electrodes (4–6 MΩ)
905 containing intracellular saline (potassium aspartate 140 mmol, KCl 1 mmol, Hepes
906 10 mmol, EGTA 1 mmol, Na_3GTP 0.5 mmol, MgATP 4 mmol, Alexafluor-568 5
907 μmol, 265 mOsm, pH 7.3). In vivo whole-cell recordings were performed in current-
908 clamp mode using a MultiClamp 700B amplifier, and digitized (NI-DAQ, National
909 Instruments) at 20 kHz. All data were acquired using the open-source software
910 Wavesurfer (https://wavesurfer.janelia.org/) running in MATLAB (MathWorks).
911 Traces were not corrected for a 13-mV liquid junction potential (Gouwens and
912 Wilson, 2009). Recordings were considered acceptable when the initial seal
913 resistance was >2 GΩ before rupture, the resting membrane potential was less

than −50 mV, and the input resistance was >50 MΩ, as the typical input resistance of the GF has been reported to be in the range of 50 to 100 MΩ.

Visual stimulation for electrophysiology and data analysis

Visual stimuli were back-projected onto a 4.5-inch diameter mylar cylindrical screen covering 180 degrees in azimuth via two DLP projectors (Texas Instruments Lightcrafter 4500) as previously described[33]. The projected images were displayed in 6-bit grayscale at 240Hz, above the flicker fusion frequency of Drosophila (100Hz; Niven et al., 2003). All stimulus frames were generated in MATLAB and presented using Psychtoolbox (http://psychtoolbox.org/). Looming stimuli were generated with the background set to white and the expanding disk (looming stimulus) set to black on the projector (5500 lx-white and 15 lx-black, measured at the position of the fly). The angular size (θ) of the stimulus subtended by the approaching object was calculated in time (t) by the following equation[66]:

$$\theta(t) = 2tan^{-1}\left(\frac{r}{vt}\right),$$

where t<0 before collision and t=0 at collision for an approaching object with a radius (r) and constant velocity (v). As previously described[66], r/v (ms) is the radius to approach speed ratio. The smaller the r/v, the more abrupt the stimulus expansion. The visual stimulus set consisted of four looming stimuli (r/v=10, 20, 40, 80 ms) starting at 10 degrees and expanding to 63 degrees in angular size and held for 1 second, displayed at −45 degrees in azimuth, 0 degrees in elevation. Each visual stimulus was presented once per trial, in a randomized order. Interstimulus intervals were set to 30 seconds to allow enough time for the GF membrane potential to return to baseline and avoid habituation. The responses to the same stimulus from two successive trials were then averaged for each fly.
Electrophysiology data distributions were evaluated using a Kolmogorov-Smirnov test. If the data were found not to follow a normal distribution, the appropriate non-parametric test was selected. Statistical comparison of GF's looming responses between two groups was performed with the Mann-Whitney U test.

Two-photon calcium imaging experiments

Imaging setup

Calcium imaging was performed with a VIVO Multiphoton Open (Intelligent Imaging Innovation, Inc.) system based on a Movable Objective Microscope (MOM, Sutter Instruments). The excitation of the sample was delivered by a Ti:Sapphire laser (Chameleon Vision I, Coherent) tuned to 920 nm with power ranging from 15 to 30 mW (depending on imaging depth). A dual axis mirror galvanometer was used for x-y laser scanning (RGG scanbox, Sutter Instrument). We imaged with a 20x water-immersion objective (W Plan-Apochromat 20x/1.0 DIC, Zeiss) and a band-pass filter (Semrock 525/40 nm) was placed in front of the photomultiplier tube (H11706P-40, Hamamatsu) to reduce the blue light from the visual display. Microscope and data acquisition were controlled by Slidebook 2024 (Intelligent Imaging Innovation, Inc.). Single plane images were sampled at 9 Hz with a spatial resolution of approximately 180 x 180 pixels (95.7 x 95.7 μm, pixel

size ≅ 0.53 μm, dwell time ≅ 2 μs). Images and external visual stimuli were synchronized *a posteriori* using frame capture markers (TTL pulses from Slidebook 2024) and stimulus events (analog outputs from the visual display) sampled with a data acquisition device (USB-6229, National Instruments) at 10 kHz.

Fly tethering and preparation for imaging

Flies were prepared and head-fixed to a custom objective stage fly holder as previously described[67]. The cuticle above the right optic lobe was removed and the brain bathed in isotonic saline. The holder with the tethered fly was placed under the objective at the center of the visual display in the horizontal plane. GCaMP7f responses of dendritic branches from individual LPLC2 neurons were recorded from a posterior view. The fly head was pitched forward pointing down at the visual display so that the fly eye's equator held a pitch angle of approximately 60° relative to the imaging plane. For each fly, we identified the most dorsocaudal dendritic arbors in the lobula plate and then moved the focal plane ~10 μm below them to start mapping the receptive field (RF) centers of dorsal LPLC2 neurons, or moved ~50 μm to probe ventral LPLC2 RFs, similarly to previous calcium imaging experiments in LPLC2[6]. Random steps (± 5 μm) between these two bracketed Z-planes were used to probe the RF centers of dorsoventrally intermediate LPLC2 neurons. Unstable recordings or recordings from preparations that did not respond during the RF scanning trials were not included in the data set.

Visual stimuli for imaging

A visual display composed of 48 8x8 dot matrix LED panels arranged in a semi-cylinder[68] was used for visual stimulation as previously described[67]. Four layers of filter (071, LEE Filters) were placed over the display to reduce its light intensity. To compensate for the angle of the eye's equator and optimize the extension of the surrounding visual context, the display was tilted forward at an angle of 30° from the horizontal plane. Visual presentation was confined to the right half of the visual field, ipsilateral to the recording site. Visual stimuli were generated and controlled using custom-written MATLAB (MathWorks) scripts that communicated to the display through the microcontroller serial port. Looming stimuli simulated an object approaching the fly at a constant velocity, equivalent to twice the inverse tangent of the ratio between object's half-size and object's approach speed (see description of electrophysiological experiments). The display background was set to 70% maximum intensity while foreground objects (looming or moving bars) were set to 0%. The set of visual stimuli was presented in random block design and repeated 2 times. Each visual stimulation lasted 4 s and was composed by 0.5 s of uniform background, and 0.5 s of visual motion followed by 3 s of static pattern. Each trial was followed by 3 s of rest in which flies faced the visual background.

Receptive field center and directional tuning

We identified an active neurite from a single neuron in the multiphoton field of view (Extended Data Fig. 9a, bottom). The RF center of that neurite was identified in real-time and subsequently scanned for directional sensitivity. We developed a custom GUI in MATLAB, which allowed for real-time modifications to stimulus

positions on the visual display. This interface enabled hand-triggered looming stimuli and the visual inspection of GCaMP responses. To identify the RF center of an LPLC2 dendritic branch, we created a rectangular grid of 48 positions across the right half of the visual display.

The positions were spaced every 5 LEDs in both horizontal and vertical directions, with each LED covering approximately 2.2° on the retina at the eye's equator. Using the GUI, the experimenter presented a looming stimulus centered at each grid position. The looming stimulus simulated a circular object with a 0.5 cm radius, starting from a distance of 50 cm and traveling at 62.5 cm/s. This caused the object to expand from 0.6° to 14° with a loom velocity (l/v) of 8 ms. If a response was visually detected, the surrounding grid positions were probed next. The position with the highest peak response was taken as the RF center for the subsequent directional tuning experiment. We tested directional selectivity by moving a dark edge outward from the center of the RF in 24 different directions (Fig. 4g, top; Extended Data Fig. 10). The edges moved at 20°/s with orientations ranging from 0° to 345° in 15° increments. Each edge subtended 15° at the eye's equator and swept 15° orthogonal to its orientation, filling a 15° black square upon completion. Additionally, a looming stimulus centered within the RF, with the same dynamics as those used for the RF scans, was included in this battery of dark moving edges.

LPLC2 position's mapping and directional sensitivity index

We sampled neurons along the DV and AP axes of the lobula and confirmed their anatomical locations by mapping the RF centers onto the fly eye (Fig. 4g, bottom). To identify the putative individual LPLC2 neurons stimulated by the RF center scans, we mapped the horizontal coordinates of their retinal positions onto the 2D retinal ommatidia lattice. We identified specific dorsal and ventral retinal ommatidia and their corresponding columnar LPLC2 in the fly connectome, verifying the recorded LPLC2 neurons' locations (Fig. 4h, Extended Data Fig. 9a).

Coordinates were calculated using a 3D reconstruction of the fly head, holder, and visual display in AutoCAD (Autodesk). We estimated the fly ommatidia with overlapping horizontal coordinates through the following steps:

(1) Identified the locations of the ommatidia pointing to positions 16 and 40 based on a Mollweide projection of 3D ommatidia directions from a microCT scan[69];

(2) Mapped these ommatidia locations onto identified visual columns of the male optic lobeconnectome[22];

(3) Used T4 neurons included in these visual columns to identify downstream LPLC2 neurons[22].

For each recording, the direction sensitivity index (DSI) was computed as follows:

$$DSI = (R_{up} - R_{down})/(R_{up} + R_{down})$$

where R_{up} is the peak response to an upward moving edge (0° direction) and R_{down} is the peak response to a downward moving edge (180° direction). The index ranges from -1 to 1, with negative values indicating downward sensitivity and positive values indicating upward sensitivity. The heatmap of the DSI for the tested positions was smoothed with a Gaussian filter (σ = 1).

Imaging data analysis

1052 Images exported from Slidebook 2024 were processed following established
1053 protocols[67]. We used a custom MATLAB toolbox developed by Ben J. Hardcastle
1054 (available at https://github.com/bjhardcastle/SlidebookObj) to correct for motion
1055 artifacts in the x-y plane and to delineate regions of interest (ROI) around individual
1056 LPLC2 neurites within the dendritic tree. For each recording, a time-series was
1057 generated by calculating the mean fluorescence intensity of pixels within the ROI
1058 (Ft) in each frame. These mean values were then normalized to a baseline value
1059 using the formula:

1060 $$\Delta F/F = (Ft - F_0)/F_0$$

1061 where F_0 is the mean of Ft during the 0.5 seconds preceding stimulus onset. This
1062 approach ensures accurate correction for motion artifacts and reliable
1063 quantification of fluorescence intensity changes in LPLC2 neurites.
1064

1065 **Statistical analysis of calcium imaging data**

1066 Given the repeated sampling and unbalanced sample sizes between groups and
1067 conditions, we employed Linear Mixed Effects (LME) models to fit the DSI values.
1068 This method maintains statistical power by avoiding averaging procedures and
1069 provides more accurate estimates of model parameters, including both fixed and
1070 random effects. The fixed effects were defined by the interaction between
1071 genotype (control/RNAi) and condition (dorsal/ventral), while the random effects
1072 were attributed to individual flies[70,71]. We modeled the data using the R package
1073 `**lme4**` assuming residuals followed a Gaussian distribution. Pairwise post-hoc
1074 comparisons of the fixed effects were conducted using t-tests with Bonferroni
1075 adjustments, implemented through the R package `**emmeans**`. Additionally, to
1076 estimate the mean DSI differences across groups and conditions without assuming
1077 a specific distribution, we performed standard bootstrap simulations with 10,000
1078 replicates using the R package `**boot**`. Smoothed heatmaps were generated with
1079 the R package '**spatstat'**.
1080

1081 ## Generation of 5xUAS-DIP-ε, -dpr13 and -beat-VI transgenic flies

1082 The coding sequences of DIP-ε, dpr13 (isoform RB), and beat-VI were cloned into
1083 a modified pJFRC5 vector (Addgene: 5XUAS-IVS-mCD8::GFP, plasmid #26218)
1084 by replacing the mCD8::GFP coding sequence. Synthesis and cloning were carried
1085 out by Genewiz, Inc. Plasmids and sequences are available upon request. Flies
1086 were generated by injecting the plasmid into embryos for recombination into attP1
1087 sites (BDSC stock #8621) by BestGene, Inc.
1088

1089 ## Generation of DIP-ε and dpr13 null alleles

1090 *DIP-ε^{null}* allele was generated as previously described[72]. Briefly, two sgRNAs were
1091 used to generate a frame-shift deletion in the DIP-ε coding sequence. High-score
1092 spacer sequences were chosen using the SSC tool[73]. Each sgRNA was cloned
1093 into pU6-2-sgRNA-short (Addgene 41700) plasmid and two plasmids were co-
1094 injected into vas-Cas9 line (BDSC # 51324) by Bestgene, Inc. Injected larvae were
1095 crossed with balancer lines, and PCR-screened in F1 for single flies carrying the
1096 deletion. A mutant stock was established from this single F1.
1097 sgRNA target sequence used for *DIP-ε^{null}* allele generation:

1098 *DIP-ε^{null}* gRNA1: GCTGTTCTGTGGTCATACGATAGC,
1099 *DIP-ε^{null}* gRNA2: CTTCAATCGATTGACGGTGGAGC
1100
1101 *dpr13^{null}* allele was similarly generated. SgRNA sequences were identified with an
1102 efficiency score above 5, as defined by the CRISPR Efficiency Predictor
1103 (https://www.flyrnai.org/evaluateCrispr/). The sgRNA sequence oligos were
1104 synthesized (Integrated DNA Technologies) and cloned into the pU6b-sgRNA-
1105 short vector[74] to generate a large ~30kb deletion spanning most of the dpr13
1106 genomic region. All pU6 vectors generated were verified by Sanger sequencing.
1107 Two plasmids were co-injected into vas-Cas9 line (BDSC# 51323) in Bestgene,
1108 Inc. Injected larvae were crossed with balancer lines, and PCR-screened in F1 for
1109 single flies carrying the deletion. A mutant stock lacking the entire coding sequence
1110 of dpr13 was established from this single F1.
1111 sgRNA target sequence used for *dpr13^{null}* allele generation:
1112 *dpr13^{null}* gRNA1: CGATATAATCCACTTGATGC,
1113 *dpr13^{null}* gRNA2: ACGTAGCAGCTCCAGGATGT.
1114 Detailed protocols are available upon request.
1115

1116 Immunohistochemistry, tissue clearing and DPX mounting

1117 Brains were dissected in ice-cold Schneider's Drosophila Medium (GIBCO
1118 #21720-024) and fixed in PBS containing 4% paraformaldehyde (PFA, Electron
1119 Microscopy Sciences 15710) for 30 minutes at room temperature (RT) or in acid-
1120 free glyoxal (Addax Biosciences) containing 5% sucrose (Sigma S9378) overnight
1121 at 4°C. Brain tissues were washed three times with PBST (PBS containing 0.5%
1122 Triton X-100, Sigma T9284) and incubated in blocking solution (PBST containing
1123 10% Normal Goat Serum, Sigma G6767) for at least 1 hour at RT before incubation
1124 with the primary antibody. Brains were incubated in primary antibody diluted in
1125 blocking solution for two nights at 4°C, washed three times in PBST for 2 hours at
1126 RT, then incubated in secondary antibodies diluted in blocking solution for two
1127 nights at 4°C. Brains were washed three times in PBST for 2 hours at RT.
1128 Subsequent mounting in DPX (EMS 13510) followed the Janelia Adult Drosophila
1129 CNS DPX mounting protocol (https://www.janelia.org/project-
1130 team/flylight/protocols). After washing from the secondary antibodies, brains were
1131 fixed with PBS containing 4% PFA for 30 minutes at RT, rinsed with PBS, and
1132 mounted on 22x22mm square No.1.5H cover glass (Thorlabs CG15CH2)
1133 previously coated with poly L-Lysine (0.078% solution in deionized water, Sigma
1134 P1524) with added 0.2% Kodak Photo-Flo 200 Solution (Electron Microscopy
1135 Sciences 74257), followed by a quick 1-2 second rinse with MilliQ water. Brains
1136 were dehydrated by placing the cover glass into baths with successively increasing
1137 ethanol (Sigma 459844) concentrations (30-50-75-95-100-100-100%, 10 minutes
1138 each), followed by three successive baths of xylene (Thermo Fisher Scientific X5-
1139 500), 5 minutes each. The glass was uniformly covered with 5-6 drops of DPX
1140 (Electron Microscopy Sciences 13510) and placed on a prepared slide between
1141 spacers made of two 22x22mm square No.2 cover glasses (Fisher Scientific 12-
1142 540B). The slide was left to dry for 24 hours in the hood, then transferred to room
1143 temperature and imaged at least 24 hours later.

Antibody information

Primary antibodies and dilutions used in this study: chicken anti-GFP (1:1000, Abcam #13970), rabbit anti-dsRed (1:200, Clontech #632496), mouse anti-Nc82 (1:20, Developmental Studies Hybridoma Bank (DSHB) Nc82), chicken anti-V5 (1:200, Fortis Life Sciences #A190-118A), mouse anti-V5 (1:500, Abcam #27671), rabbit anti-HA (1:200, Cell Signaling Technology #3724), rabbit anti-FLAG (1:200, Abcam #205606), rat anti-N-Cadherin (1:40, DSHB MNCD2), and anti-GFP nanobody (1:200 for expansion microscopy, 1:500 for confocal microscopy, NanoTag Biotechnologies #N0304-At488-L). Secondary antibodies and dilutions used in this study: goat anti-chicken AF488 (1:500, Invitrogen #A11039), goat anti-mouse AF488 (1:500, Invitrogen #A21131), goat anti-rabbit AF568 (1:500, Invitrogen #A11011), goat anti-mouse AF568 (1:500, Thermo Fisher #A11031), goat anti-mouse AF647 (1:500, Jackson ImmunoResearch #115-607-003), goat anti-mouse CF633 (1:500, Biotium #20250-1), and goat anti-rat AF647 (1:500, Jackson ImmunoResearch #112-605-167).

Confocal image acquisition and processing

Immunofluorescence images were acquired using a Zeiss LSM 880 confocal microscope with 488 nm, 561 nm, and 633 nm lasers using Zen digital imaging software with a Plan-Apochromat 63x/1.4 Oil DIC M27 objective. Serial optical sections were obtained from whole-mount brains with a typical resolution of 1024µm × 1024µm × 0.5µm. Image stacks were exported to either Fiji software or Imaris 10.1 (Oxford Instruments) for level adjustment, cropping, removal of off-target brain regions and background noise, and 3D volume reconstructions.

Analysis of neuroanatomical data from confocal image stacks

To measure the axo-dendritic overlap volume between LPLC2 axons and GF dendrites, confocal image stacks of colocalized LPLC2 glomeruli and GF dendrites were imported into Imaris 10.1 for 3D reconstruction using the Surfaces tool to create masks for membranes of pre- and postsynaptic neurons from the corresponding channels. A Surfaces Detail value of 1 micron was used for both LPLC2 and GF surfaces to ensure accurate reconstruction. Background subtraction was applied with a diameter of the largest sphere that fits into the object set to 1 micron to minimize noise and non-specific signals. For experiments using GF-GAL4, the background subtraction threshold was set to 1 for the GF and 2 for LPLC2, while for experiments using LPLC2-GAL4, the threshold was set to 0.7 for the GF and 2 for LPLC2. The overlap volume between the two reconstructed surfaces was then assessed to quantify the spatial relationship between the LPLC2 axons and GF dendrites. To measure LoP4 dendritic branch length in sparsely labeled LPLC2 neurons, corresponding image stacks were imported into Fiji, rotated so that LoP3 and LoP4 branches were seen as antiparallel, and the distance from the point of bifurcation to the most distal tip of the LoP4 branch was measured along Lop4.

ExLSM and HCR-FISH

1190 Tissue staining, gelation and expansion for ExLSM
1191 Brains were dissected in ice-cold Schneider's Drosophila Medium (GIBCO
1192 #21720-024) and fixed in PBS containing 4% paraformaldehyde (PFA, Electron
1193 Microscopy Sciences 15710) for 30 minutes on ice. Brains were then washed three
1194 times with PBST (PBS containing 0.5% Triton X-100, Sigma T9284) on ice and left
1195 in PBST containing anti-GFP nanobody (NanoTag Biotechnologies #N0304-
1196 At488-L) overnight at 4°C. All samples were processed using a protein and RNA
1197 retention ExM protocol with minor modifications[75] and adjustments for the fly
1198 brain[44]. All solutions used for ExLSM and HCR-FISH were prepared with
1199 DNase/RNase free distilled water (Thermo Fisher #10-977-023). After staining,
1200 brains were washed three times with PBST on ice and left in MOPS buffer3 (20
1201 mM γ-(N-Morpholino) propanesulfonic acid, Fisher Scientific cat# AC327661000,
1202 pH 7.7) containing 1:100 AcX stock solution (acryloyl-X, SE Invitrogen,
1203 Cat#A20770 at 10 mg/mL in anhydrous DMSO (Sigma-Aldrich, Cat# 276855)) and
1204 1:2 Melphalan X[76] solution (made by combining 2.5 mg/mL Melphalan, Cayman
1205 Chemical Company #16665 with 10 mg/mL AcX overnight shaking at room
1206 temperature) overnight at 37°C. Brains were then washed three times with 1xPBS.
1207 A gelation chamber was created by applying a Press-to-Seal silicone gasket
1208 (Invitrogen, Cat# P24740) to a glass slide, which was then coated with the PLL
1209 solution. AcX-treated brains were immobilized on the PLL surface, up to nine per
1210 gasket. Gelation solution was prepared just before gelation to prevent premature
1211 gel polymerization on ice by adding 10 µL each of 4-hydroxy-TEMPO at 0.5% (w/v)
1212 (Sigma-Aldrich, Cat# 176141), TEMED (N,N,N′,N′-Tetramethylethylenediamine at
1213 10% (v/v) (Sigma-Aldrich, Cat# T7024), and ammonium persulfate at 10% (w/v)
1214 (Sigma-Aldrich, Cat# A3678) to 470 µL of monomer stock solution (11.5 mL
1215 sodium acrylate stock at 4M, prepared by neutralizing 5.5 mL acrylic acid (99%
1216 purity; Sigma-Aldrich, Cat# 147230) with 10N NaOH using a water bath and fume
1217 hood, in a total volume of 20 mL; 2.5 mL acrylamide stock at 50% (w/v), Sigma-
1218 Aldrich, Cat# A9099; 7.5 mL bis-acrylamide stock at 1% (w/v), Sigma-Aldrich, Cat#
1219 M7279; 18 mL 5 M NaCl, Sigma-Aldrich, Cat# S5150). Brains were washed with
1220 gelation solution, and then the gelation chamber was filled with ~200 µL of gelation
1221 solution and incubated on ice for 25 minutes. The gelation chamber was then
1222 sealed with a cover slip and placed in a 37°C incubator to gel and cure for 2 hours.
1223 Gelation chambers were disassembled, and individual gels were trimmed close to
1224 each brain. Gels were trimmed to a right trapezoid shape to ease specimen
1225 orientation. Gels were transferred into 12-well plates (Laguna Scientific #4624-12)
1226 and incubated with proteinase K (NEB, Cat# P8107S) diluted 1:100 (v/v) in
1227 proteinase K digestion buffer (0.5% Triton X-100, 50 mM NaCl, 1 mM EDTA, and
1228 50 mM Tris pH 8) with shaking overnight at room temperature. This resulted in ~2x
1229 gel expansion.
1230
1231 HCR-FISH
1232 The HCR-FISH protocol was adapted from Wang et al[76] with minor
1233 optimizations for the fly brain[44]. Following digestion with proteinase K, gels
1234 with embedded brains were washed 3 times with PBS, transferred into 24-
1235 well plates (Laguna Scientific #4624-24), and digested with DNase diluted

1236 in RDD buffer (RNase-Free DNase Set, Qiagen #79254) to limit DAPI signal
1237 to RNA only and facilitate subsequent analysis for 2 hours at 37°C. After
1238 three washes in PBS, gels were equilibrated in Probe Hybridization Buffer
1239 (Molecular Instruments, Inc.) for 30 minutes at 37°C, and then transferred to
1240 new 24-well plates containing custom-designed probes (Molecular
1241 Instruments, Inc.) diluted in pre-warmed Probe Hybridization Buffer (1 µL of
1242 1 µM stock probe solution per 200 µL of buffer) and left shaking overnight at
1243 37°C. The following day, gels were washed 4 times with pre-warmed Probe
1244 Wash Buffer (Molecular Instruments, Inc.) for 20 minutes at 37°C, then
1245 washed twice for 5 minutes with SSCT buffer (SSC, Thermo Fisher
1246 #AM9763 with 0.05% Triton X-100) at room temperature and transferred to
1247 new 24-well plates with HCR Amplification buffer (Molecular Instruments,
1248 Inc.) for equilibration. Hairpins (HCR Amplifiers, Molecular Instruments, Inc.)
1249 conjugated with AF546 or SeTau647 dyes were diluted in Amplification
1250 Buffer (2 µL of each hairpin per 100 µL of buffer), heat-activated in a thermal
1251 cycler (90 seconds at 95°C), removed, and kept for 30 minutes at room
1252 temperature in the dark. After 30 minutes, the hairpins were added to the
1253 24-well plates with gels (300 µL per well) and incubated with shaking at room
1254 temperature in the dark for 3 hours. The hairpin solution was then removed,
1255 and the gels were washed 4 times with SSCT and 2 times with SSC for 10
1256 minutes at RT in the dark. Gels were subsequently stored at 4°C in SSC
1257 until final expansion.
1258

1259 Sample mounting

1260 Samples were expanded to ~3X in 0.5x PBS containing 1:1000 SYTO-DAPI
1261 (Thermo Fisher S11352) at room temperature for 2 hours before mounting onto
1262 PLL-coated coverslips (see description for DPX mounting above). The coverslips
1263 were then bonded with Bondic UV-curing adhesive (Bondic starter kit, Bondic) onto
1264 a custom fabricated sample holder (Janelia Tech ID 2021-021) to be suspended
1265 vertically in the imaging chamber. Mounted samples were imaged in 0.5x PBS with
1266 1:10,000 SYTO-DAPI after a minimum of 1 hour of equilibration in the imaging
1267 chamber. Unexpanded gels were stored at 4°C in 1X PBS + 0.02% sodium azide
1268 (Sigma-Aldrich, Cat# S8032) for up to 14 days before final expansion and imaging.
1269

1270 Light-sheet microscopy

1271 Images were acquired on a Zeiss LS7 microscope equipped with 405 nm, 488 nm,
1272 561 nm, and 638 nm lasers. Illumination optics with a 10x/0.2 NA were used for
1273 excitation (Zeiss, Cat# 400900-9020-000). Detection was performed using a W
1274 Plan-Apochromat 20x/1.0 DIC M27 water immersion objective (Zeiss, Cat#
1275 421452-9700-000). The LS7 optical zoom was set to 2.5x, resulting in a total
1276 magnification of 50x. DAPI and AF546 dyes were simultaneously excited by the
1277 405 nm and 561 nm laser lines, and emission light was separated by a dichroic
1278 mirror SBS LP 510 with emission filters BP 420-470 (Zeiss, Cat# 404900-9312-
1279 000) and a modified BP 527/23 (Chroma, Cat# ET672/23m). Similarly, AF488 and

1280 SeTau647 dyes were simultaneously excited via 488 nm and 638 nm, and the
1281 emission was split through a dichroic SBS LP 560 with emission filters BP 505-545
1282 and LP 660 (Zeiss, Cat# 404900-9318-000). To eliminate laser transmission, a
1283 405/488/561/640 laser blocking filter (Zeiss, Cat# 404900-9101-000) was added
1284 to the emission path. Images were captured using dual PCO.edge 4.2 detection
1285 modules (Zeiss, Cat# 400100-9060-000) with a 50 msec exposure time. Filter and
1286 camera alignment were manually calibrated prior to each imaging session. Image
1287 volumes were acquired at optimal Z-step and light-sheet thickness, and the Pivot
1288 Scan feature was used to reduce illumination artifacts by sweeping the light-sheet
1289 in the xy-plane. The LS7 microscope was operated using ZEN Black 3.1
1290 (v9.3.6.393).
1291

1292 ## Analysis of HCR-FISH data from ExLSM Image Stacks

1293 The full details of our analysis are available in our previous publication[45]. The
1294 acquired z-stacks, stored in CZI format, were imported and pre-processed to
1295 remove noise and artifacts generated by the imaging modality. These artifacts
1296 included limited channel contrast, variations in contrast from image to image within
1297 a dataset, background noise fluctuations due to both intra-channel variations and
1298 inter-channel crosstalk, and localized brightness changes from varying fluorophore
1299 concentrations within and among stained nuclei. Pre-processing involved the
1300 following steps: full-scale contrast stretching (FSCS) to normalize luminosity
1301 across different channels, local background removal using a 3D Gaussian filter, a
1302 second FSCS to adjust for any contrast loss due to background removal, and a
1303 final median filter to remove any remaining localized noise. These pre-processed
1304 stacks served as the starting point for instance segmentation of the nuclei. First,
1305 the nuclei centers were identified using a Laplacian-of-Gaussian (LoG) filter. Then,
1306 the imaged volume was subdivided into 3D Voronoi cells, using the detected
1307 centers as seeds and Euclidean distance. Each cell contained one nucleus, which
1308 was segmented using a threshold obtained by minimizing an energy functional
1309 designed to find the optimal surface separating the nucleus from the surrounding
1310 cytoplasm. Once each nucleus was segmented, the FISH puncta were identified
1311 within the 3D volume associated with it using a LoG filter, and only the puncta
1312 within the nucleus region and its immediate surrounding volume were counted.
1313 Pre-processed products, segmented nuclei features, associated FISH puncta, and
1314 their features were stored for further analysis. Puncta counts were normalized by
1315 the maximum count for each brain. The significance of gene expression
1316 relationships inferred from HCR-FISH (Fig. 2) was assessed using both a linear
1317 regression model and a multi-level negative binomial generalized linear mixed
1318 model, accounting for inter-animal heterogeneity: random effects were attributed
1319 to individual animals (Supplemental Table 2). The package was written in Python,
1320 is open-source, and available for download at
1321 https://github.com/avaccari/DrosophilaFISH.
1322

1323 ## Genetic Intersection of cell types and genes

1324 To assess gene expression levels within LPLC2 and LPLC1 cell types, we used a
1325 combination of GAL4 and LexA binary expression systems. Expression of a

1326 LexAop-FRT-stop-FRT-membrane marker controlled by a cell-type-specific LexA
1327 driver was blocked until the FRT-stop-FRT cassette was excised by a Flippase,
1328 driven by a gene-specific T2A-GAL4 driver line[77]. Additionally, an unconditional
1329 membrane marker controlled by the same LexA driver visualized the entire cell
1330 population. The list of fly stocks used is available in Supplemental Table 1.
1331

1332 Sparse labeling of neuronal populations

1333 To visualize single cell morphology of LPLC2 dendrites in the lobula plate
1334 (Fig 4) and for dorsoventral HCR-FISH analysis (Ext. Data Fig. 3), we used
1335 MultiColor FlpOut (MCFO)[78], a genetic tool for sparse labeling individual cells
1336 within a neuronal population acting downstream of a given Gal4 driver. 24h pupae
1337 were heat shocked in a 37°C water bath for ten minutes to achieve the labeling of
1338 one LPLC2 neuron per hemibrain om average.
1339

1340 Analysis of the Flywire Connectome reconstruction

1341 To analyze the *Flywire* connectome, we developed an open-source Python
1342 package, available at https://github.com/avaccari/DrosophilaCon. The primary
1343 library used by *DrosophilaCon* to interface with the *FlyWire* connectome is
1344 *fafbseg*[32,33] (version 3.0.0). This package enables users to specify the labels of
1345 "source" and "target" neurons and generates a connectivity diagram where target
1346 neurons are color-coded based on the total count of synapses with the source
1347 neurons. Once the labels are specified, the package queries the latest available
1348 annotations to identify all neurons matching (or containing) the labels. The primary
1349 sources of annotation used to identify the neurons are:
1350 (1) Free-form community annotations provided through the *neuroglancer* user
1351 interface (https://github.com/google/neuroglancer).
1352 (2) Systematic annotations for the entire brain[33].
1353 (3) Systematic cell types for the right optic lobe[79].
1354 Next, the latest version of the *FlyWire* production dataset is queried for the
1355 adjacency matrix representing the connectivity between each neuron in the source
1356 and each neuron in the target for the selected side of the brain. This information is
1357 returned as an adjacency table, providing the counts of synapses between each
1358 source-target pair. There are two versions of the synapse datasets: one filtered by
1359 synaptic cleft and one unfiltered. We used the unfiltered dataset because the
1360 filtered version applied a fixed threshold for distance, resulting in reduced synapse
1361 counts. The adjacency table was used to evaluate the total synapse counts for
1362 each target neuron. These counts were normalized by the maximum count
1363 observed across all target neurons. The mesh representation for each identified
1364 target neuron was downloaded from the *FlyWire* dataset, skeletonized to optimize
1365 processing, and displayed with color-coding corresponding to the normalized
1366 synapse count, allowing for comparison across different source-target pairs.
1367

1368 Statistical analysis

1369 All statistical analyses were performed using RStudio 1.4.1103, MATLAB,
1370 or Prism 9.2.0 (GraphPad). Significance levels were defined as follows: $p < 0.05$,
1371 $*p < 0.01$, $**p < 0.001$, $***p < 0.0001$ for all figures. Statistical tests were chosen

based on data distribution, which was assessed using the Kolmogorov-Smirnov test in R with a p-value threshold of <0.05 for normality. Two groups of normally distributed data sets were tested for statistically significant differences using unpaired t-tests with Welch's correction for non-identical variance. For comparisons involving more than two groups, we employed either one-way ANOVA followed by Tukey's HSD test for post-hoc pairwise comparisons or the Kruskal-Wallis test followed by Dunn's multiple comparisons post-hoc test with Bonferroni correction. Binary data were compared using chi-squared tests. Detailed statistical analyses for behavioral data, HCR-FISH data, and neuroanatomical data are described in Supplementary Table 2. All other statistical tests, number of replicates, significance levels, and other elements of the statistical analysis are reported within the corresponding Methods and Results sections and/or Figure Legends. No data were excluded from the analysis unless specified in the corresponding Methods section. All measurements were taken from distinct samples.

Data availability

The datasets generated and/or analyzed during the current study are available from the corresponding authors upon reasonable request. For further information regarding any resources and reagents, please contact S. Lawrence Zipursky (lzipursky@mednet.ucla.edu) and Gwyneth M. Card (gc3017@columbia.edu). Source Data are provided with this paper.

Code availability

The code for single-cell RNA-seq analysis is available at https://github.com/kurmangaliyev-lab. Our code for the analysis of Flywire and "hemibrain" connectome reconstructions is available at https://github.com/avaccari/DrosophilaCon and https://github.com/avaccari/DrosophilaVPNWiring, respectively. Code used to analyze HCR-FISH data is available at https://github.com/avaccari/DrosophilaFISH. Code related to calcium imaging experiments is available at https://osf.io/z7xfk/. All other code can be made available from the corresponding authors upon request.

Acknowledgements

We thank the Bloomington Stock Center (NIH P40OD018537), Vienna *Drosophila* Research Center and Janelia Fly Facility for providing fly stocks. We also thank the UCLA BSCRC Sequencing Core and the UCLA TCGB core for help with library preparation and scRNA-seq; the UCLA BSCRC FACS core for assistance with FACS purification. We thank members of the Flywire Consortium for connectome annotation in the FAFB dataset. We thank all members of the Zipursky lab for advice and comments on the manuscript. This work was supported by the HHMI-Helen Hay Whitney Foundation (M.D.), NEI K99EY036123 (M.D.), NEI R01EY026031 (M.F.), and NINDS R01NS118562 (C.R.v.R) S. L. Z. and G.M.C. are investigators of the Howard Hughes Medical Institute.

Author Contributions

Conceptualization and Methodology: M.D., Y.Z.K, C.R.v.R., M.A.F., G.M.C., S.L.Z.; Investigation & Data collection: M.D., Y.Z., G.F., H.J., Parmis S. Mirshahidi, A.R., R.H.H., C.L. and Pegah S. Mirshahidi; Data analysis: M.D., Y.Z.K., A.V., Y.Z., G.F., H.J., F.X., B.W.H.; Writing, reviewing and editing.; M.D., Y.Z.K., Y.Z., G.F., H.J., C.R.v.R., G.M.C. and S.L.Z.; Supervision and funding acquisition: S.L.Z, G.M.C., C.R.v.R., M.A.F., M.D.

Ethics Declarations

Competing interests

The authors declare no competing interests

Figure 1

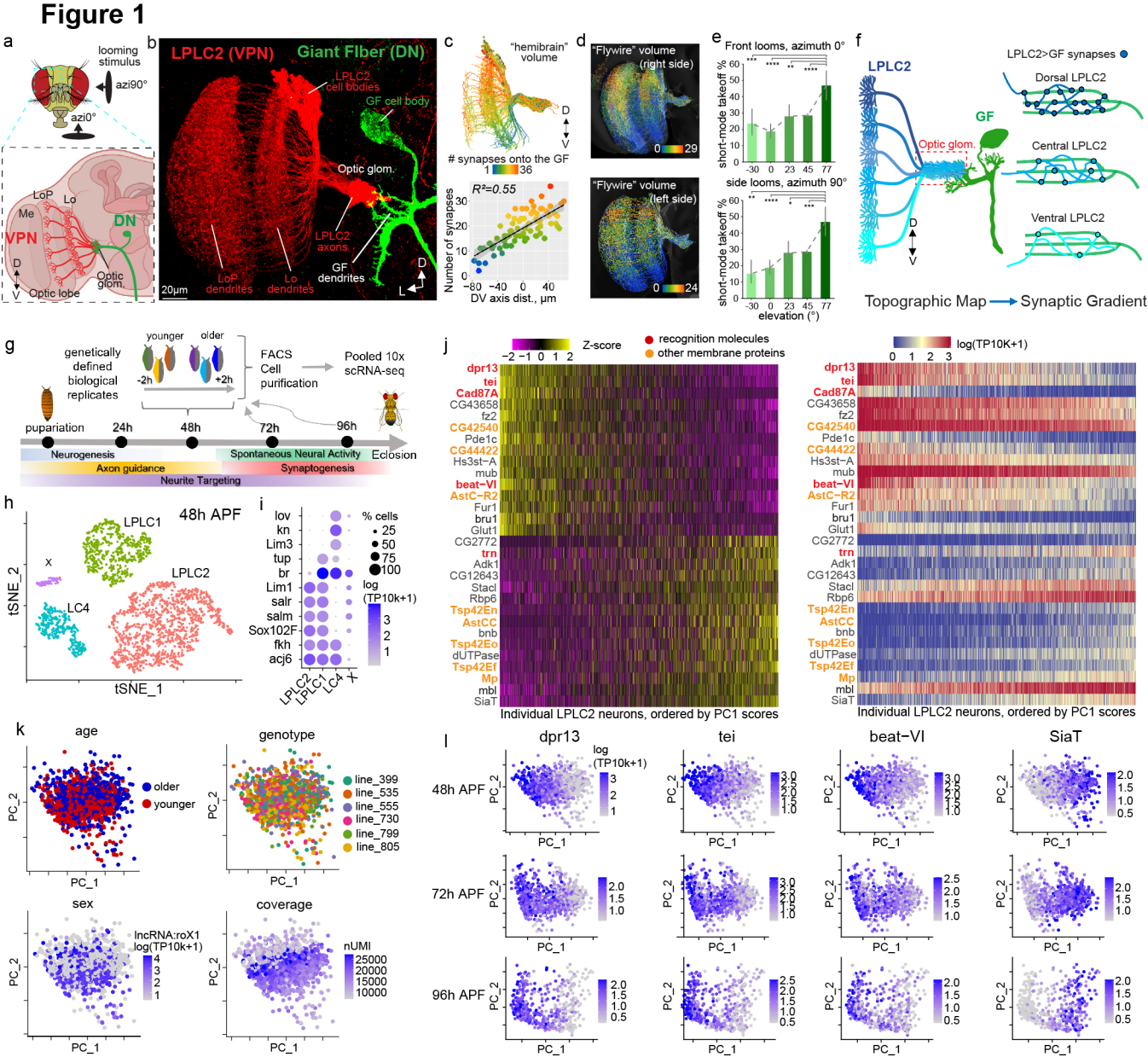
a
looming stimulus
azi90°
azi0°
LoP
Lo
Me
VPN
DN
D
V
Optic glom.
Optic lobe
b
LPLC2 (VPN)
Giant FIber (DN)
LPLC2 cell bodies
GF cell body
Optic glom.
LPLC2 axons
GF dendrites
LoP dendrites
Lo dendrites
20μm
c
"hemibrain" volume
synapses onto the GF
1 36
R²=0.55
Number of synapses
DV axis dist., μm
d
"Flywire" volume (right side)
"Flywire" volume (left side)
e
Front looms, azimuth 0°
short-mode takeoff %
side looms, azimuth 90°
elevation (°)
f
LPLC2
GF
Optic glom.
LPLC2>GF synapses
Dorsal LPLC2
Central LPLC2
Ventral LPLC2
Topographic Map → Synaptic Gradient
g
genetically defined biological replicates
younger
older
-2h
+2h
FACS Cell purification
Pooled 10x scRNA-seq
pupariation
24h
48h
72h
96h
Eclosion
Neurogenesis
Spontaneous Neural Activity
Axon guidance
Synaptogenesis
Neurite Targeting
h
48h APF
LPLC1
LPLC2
LC4
X
tSNE_1
tSNE_2
i
% cells
25
50
75
100
log (TP10k+1)
lov
kn
Lim3
tup
br
Lim1
salr
salm
Sox102F
fkh
acj6
LPLC2
LPLC1
LC4
X
j
Z-score
recognition molecules
other membrane proteins
log(TP10K+1)
dpr13
tei
Cad87A
CG43658
fz2
CG42540
Pde1c
CG44422
Hs3st-A
mub
beat-VI
AstC-R2
Fur1
bru1
Glut1
CG2772
trn
Adk1
CG12643
Stacl
Rbp6
Tsp42En
AstCC
bnb
Tsp42Eo
dUTPase
Tsp42Ef
Mp
mbl
SiaT
Individual LPLC2 neurons, ordered by PC1 scores
k
age
older
younger
genotype
line_399
line_535
line_555
line_730
line_799
line_805
sex
lncRNA:roX1 log(TP10k+1)
coverage
nUMI
PC_1
PC_2
l
dpr13
tei
beat-VI
SiaT
log (TP10k+1)
48h APF
72h APF
96h APF

Fig. 1: Gradients of recognition molecules correlate with synaptic gradients and behavior in Visual Projection Neurons

a-d, Anatomy

a, Visual Projection Neurons (VPN) have dendrites that cover the lobula (Lo), lobula plate (LoP) or both neuropils of the fly optic lobe. Axons converge on optic glomeruli in the central brain innervated by dendrites of target neurons, e.g., Descending Neurons (DN); D-dorsal, V-ventral, L-lateral.

b, Confocal projection (posterior view) of LPLC2 VPNs and the Giant Fiber DN.

c, Top: EM-based reconstructions of LPLC2 neurons (posterior view) from the "hemibrain" volume, color-coded by the number of synapses their axons make onto the GF. Bottom: linear regression of LPLC2-GF synapse numbers as a function of LPLC2 dendrite position along the DV axis of the visual space. Dots, individual LPLC2 neurons (colored as above). Shaded region, 95% confidence interval).

d, same as (**e**, top), inferred from the Flywire volume (left and right sides)

e, **Behavior**: GF-mediated short-mode (<7 ms sequence duration) takeoffs in response to frontal (0°) and lateral (90°) looms at various elevations. Error bars, 95% confidence intervals.

f, **Summary**: Transformation of retinotopic dendritic maps into axonal synaptic gradients between LPLC2 and the GF without axonal retinotopy.

g-l, **Identification of gene expression gradients in VPNs**.

g, Single-cell RNA-sequencing experimental design (See Methods).

h-i, t-SNE plots of 48h APF dataset (**h**) LPLC2, LPLC1, and LC4 neurons were annotated based on the expression of known marker genes (**i**). X, unknown ectopic cell type.

j, Heatmaps of the expression patterns of the top 30 genes with the highest contribution (loading) to Principal Component 1 (PC1) across LPLC2 neurons at 48h APF (PCA was performed separately on LPLC2 neurons); genes (rows) ordered by their loadings to PC1; cells (columns) ordered by their PC1 scores; expression patterns colored by scaled expression levels (left) and original log-normalized expression values (right).

k, Distributions of LPLC2 neurons at 48h APF along PC1 and PC2 (PCA plots) colored by developmental age, genotype, sex (male-specific transcript), and coverage.

l, PCA plots of LPLC2 neurons at 48, 72, and 96h APF, colored by the expression levels of the select genes from (**j**). Differential expression of these genes is consistent over time.

Figure 2

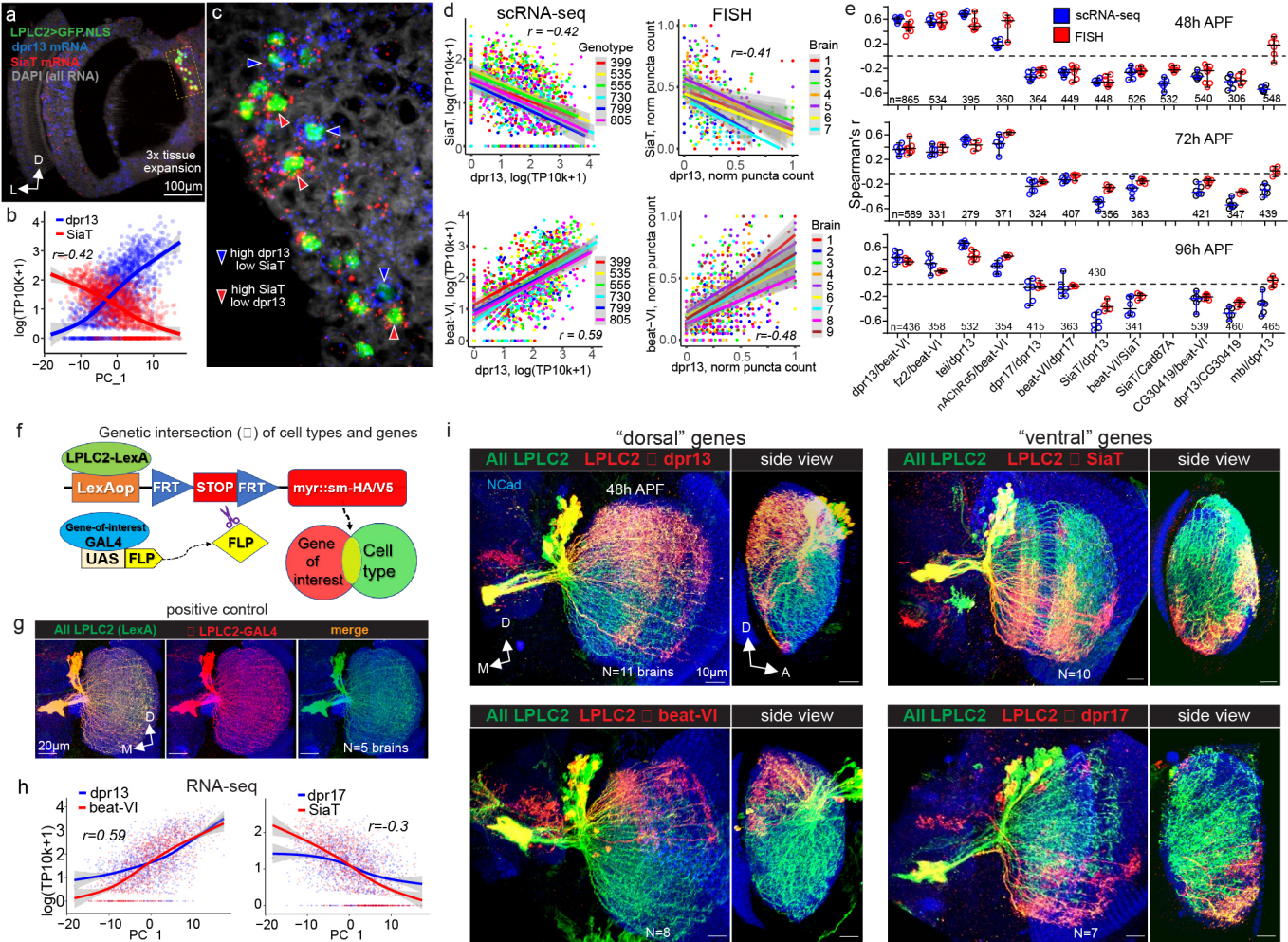
a
LPLC2>GFP.NLS
dpr13 mRNA
SiaT mRNA
DAPI (all RNA)
3x tissue expansion
100µm
D
L
b
dpr13
SiaT
r=-0.42
log(TP10K+1)
PC_1
c
high dpr13 low SiaT
high SiaT low dpr13
d
scRNA-seq
r = −0.42
Genotype
399
535
555
730
799
805
SiaT, log(TP10k+1)
dpr13, log(TP10k+1)
FISH
r=-0.41
Brain
SiaT, norm puncta count
dpr13, norm puncta count
r = 0.59
beat-VI, log(TP10k+1)
r=-0.48
beat-VI, norm puncta count
e
scRNA-seq
FISH
48h APF
72h APF
96h APF
Spearman's r
n=865 534 395 360 364 449 448 526 532 540 306 548
n=589 331 279 371 324 407 356 383 421 347 439
n=436 358 532 354 415 363 430 341 539 460 465
dpr13/beat-VI
fz2/beat-VI
tei/dpr13
nAChR5/beat-VI
dpr17/dpr13
beat-VI/dpr17
SiaT/dpr13
beat-VI/SiaT
SiaT/Cad87A
CG30419/beat-VI
dpr13/CG30419
mbl/dpr13
f
Genetic intersection (□) of cell types and genes
LPLC2-LexA
LexAop
FRT
STOP
FRT
myr::sm-HA/V5
Gene-of-interest
GAL4
UAS
FLP
FLP
Gene of interest
Cell type
g
positive control
All LPLC2 (LexA)
□ LPLC2-GAL4
merge
20µm
D
M
N=5 brains
h
RNA-seq
dpr13
beat-VI
r=0.59
log(TP10k+1)
PC 1
dpr17
SiaT
r=-0.3
PC 1
i
"dorsal" genes
"ventral" genes
All LPLC2
LPLC2 □ dpr13
side view
NCad
48h APF
D
M
N=11 brains
10µm
D
A
All LPLC2
LPLC2 □ SiaT
side view
N=10
All LPLC2
LPLC2 □ beat-VI
side view
N=8
All LPLC2
LPLC2 □ dpr17
side view
N=7

1509 **Fig. 2: Gradients of recognition molecules align with synaptic gradients**
1510 **a-e, FISH analysis.**
1511 **a,** Light sheet projection of the expanded *Drosophila* optic lobe (48h APF) with
1512 labeled LPLC2 nuclei and transcripts of dpr13 and SiaT.
1513 **b,** Anti-parallel expression of dpr13 and SiaT across LPLC2 neurons at 48h APF
1514 (inferred from scRNAseq, along PC1). Fitted lines, trends of gene expression
1515 changes along PC1; shaded areas, 95% confidence intervals. r, Spearman's rank
1516 correlation coefficient.
1517 **c,** Single slice (0.5μm thick) from the projection in (**a**) (zoomed into the dashed
1518 rectangular region); arrows indicate individual LPLC2 neurons expressing
1519 markedly different levels of dpr13 and SiaT.
1520 **d,** Comparison of scRNA-seq (left) and FISH (right) measuring correlation in
1521 expression for two pairs of graded genes: dpr13/SiaT (top) and dpr13/beat-VI
1522 (bottom) across LPLC2 neurons at 48h APF. Fitted lines, linear relationship
1523 between the expression levels of two genes for each brain (FISH) or each wild-
1524 type genotype (scRNA-seq). Shaded regions, 95% confidence intervals.
1525 **e,** Comparison of RNA-seq and HCR-FISH measuring correlation in expression for
1526 twelve pairs of genes at three time points across LPLC2 neurons. Individual dots
1527 represent Spearman's rank correlation coefficients for each brain (FISH) and each
1528 genotype (scRNA-seq). Error bars, means ±95% confidence intervals; n, total
1529 number of neurons tested using FISH.
1530 **f-i, GAL4-reporter analysis.**
1531 **f,** Genetic approach to visualize a subset of neurons within a VPN cell type
1532 population expressing a specific gene at a particular time point.
1533 **g**, Positive control for (**f**). LPLC2-LexA genetically intersected with LPLC2-GAL4,
1534 results in labeling of all LPLC2 neurons.
1535 **h**, Correlation between expression levels of dpr13/beat-VI and dpr17/SiaT
1536 (inferred from scRNA-seq), along PC1 across the LPLC2 population at 48h APF.
1537 **i**, Subsets of LPLC2 neurons expressing dpr13, dpr17, beat-VI and SiaT at 48h
1538 APF. D, dorsal; M, medial; A, anterior.
1539
1540
1541
1542
1543
1544
1545
1546
1547
1548
1549
1550
1551
1552
1553

Figure 3

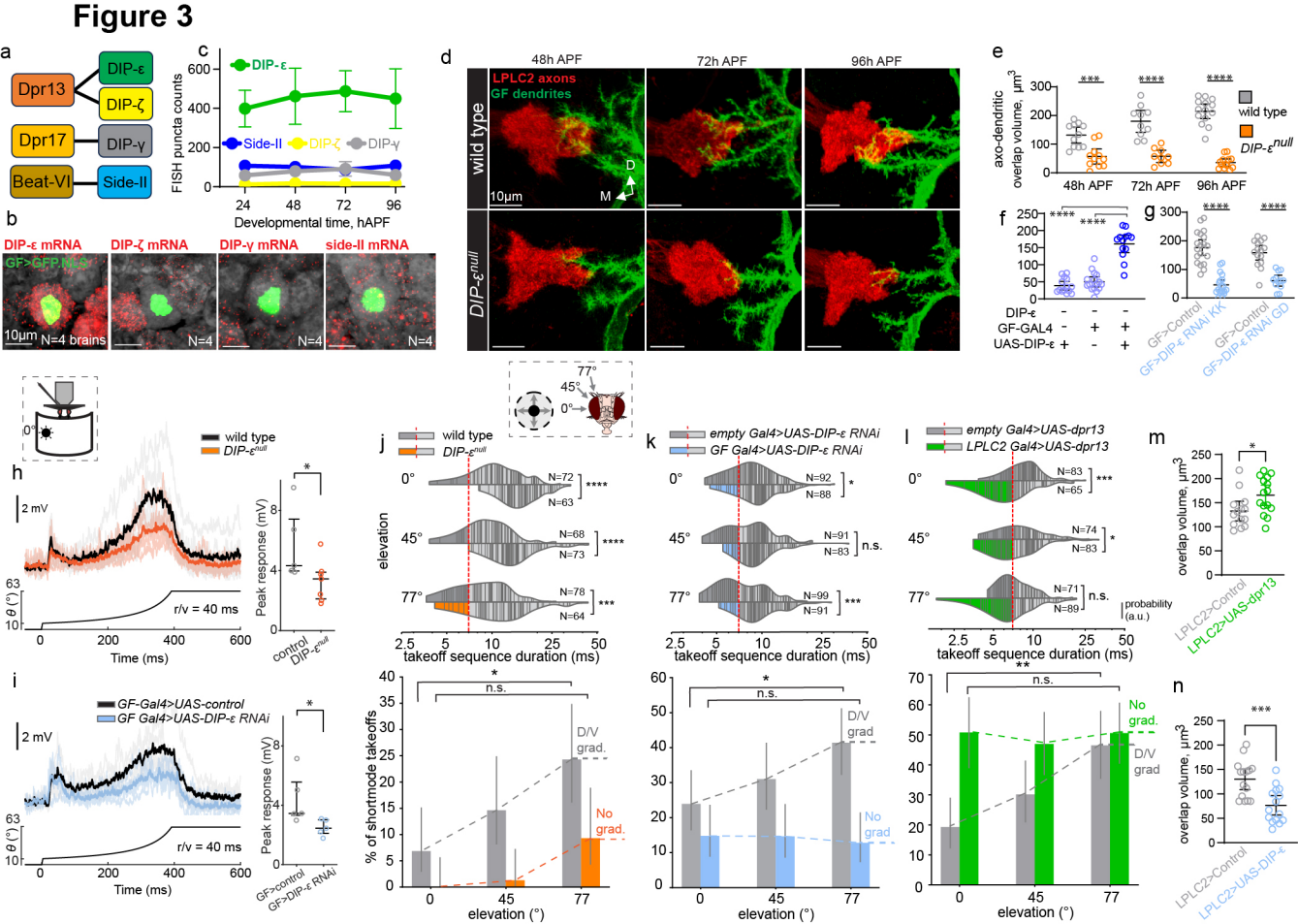
a
Dpr13
DIP-ε
DIP-ζ
Dpr17
DIP-γ
Beat-VI
Side-II
b
DIP-ε mRNA
DIP-ζ mRNA
DIP-γ mRNA
side-II mRNA
GF>GFP,NLS
10µm
N=4 brains
N=4
c
DIP-ε
Side-II
DIP-ζ
DIP-γ
FISH puncta counts
Developmental time, hAPF
d
48h APF
72h APF
96h APF
LPLC2 axons
GF dendrites
wild type
DIP-ε null
10µm
D
M
e
axo-dendritic overlap volume, µm3
wild type
DIP-ε null
f
DIP-ε
GF-GAL4
UAS-DIP-ε
g
GF>Control
GF>DIP-ε RNAi KK
GF>DIP-ε RNAi GD
h
wild type
DIP-ε null
2 mV
θ (°)
r/v = 40 ms
Time (ms)
Peak response (mV)
control
DIP-ε null
i
GF-Gal4>UAS-control
GF Gal4>UAS-DIP-ε RNAi
GF>control
GF>DIP-ε RNAi
j
wild type
DIP-ε null
elevation
takeoff sequence duration (ms)
% of shortmode takeoffs
D/V grad.
No grad.
elevation (°)
k
empty Gal4>UAS-DIP-ε RNAi
GF Gal4>UAS-DIP-ε RNAi
l
empty Gal4>UAS-dpr13
LPLC2 Gal4>UAS-dpr13
probability (a.u.)
m
overlap volume, µm3
LPLC2>Control
LPLC2>UAS-dpr13
n
LPLC2>Control
LPLC2>UAS-DIP-ε

Fig. 3: A gradient of DIP-ε::Dpr13 recognition molecules controls a looming escape synaptic gradient in LPLC2 neurons

a, Protein interaction map showing molecular binding partners of most differentially expressed recognition molecules in LPLC2.

b, Light sheet projections of the GF (nuclear marker). Red puncta, mRNA of designated genes assessed through HCR-FISH.

c, Candidate gene expression levels (FISH puncta counts) in the GF throughout development. Error bars, means with ±95% confidence intervals.

d, Confocal projections of LPLC2 axon terminals and the GF dendrites in wild type and *DIP-ε^{null}* animals throughout development. M, medial; D, dorsal.

e-g, Comparison of LPLC2-GF axo-dendritic overlap volume (see Methods) between controls and in *DIP-ε^{null}* animals (**e**), DIP-ε rescue in the GF (**f**), and GF expressing two different DIP-ε RNAi (**g**).

h, Whole-cell patch-clamp recordings in the GF during presentations of looming stimuli. Left: GF responses to looming stimuli, r/v = 40ms. Control (average: black, individual fly: grey) and *DIP-ε^{null}* (average: orange, individual fly: light orange) traces are overlayed. Looming stimulus profile over time is displayed below the GF responses. Right: Quantification of expansion peak amplitudes from individual flies; each data point represents the mean value of two recordings per animal.

i, Same as (**h**) for controls (grey) and animals overexpressing DIP-ε RNAi in the GF (light blue).

j, Top: Violin plots of takeoff sequence durations for lateral stimuli (90°) at different elevations (0°, 45°, 77°) in wild-type and *DIP-ε^{null}* animals. Lines, single takeoffs. Short-mode (<7 ms, grey for wild-type, orange for *DIP-ε^{null}*) and long-mode (≥7 ms, grey) durations separated by a red dashed line. N = number of flies. Bottom: short-mode takeoff percentages at different elevations. Error bars, 95% confidence intervals. Dashed lines, wild-type DV gradient (grey) and eliminated DV gradient in *DIP-ε^{null}* (orange).

k, Same as (**j**) for controls (grey) and animals overexpressing DIP-ε RNAi in the GF (light blue). .

l, Same as (**j**) for controls (grey) and animals overexpressing dpr13 in LPLC2 neurons (green).

m, Comparison of LPLC2-GF axo-dendritic overlap volume in control animals, and animals expressing overexpressing dpr13 in LPLC2

n, Same as (**m**), for control animals, and animals overexpressing DIP-ε in LPLC2.

panels **e**, **f**, **g**, **m**, **n**: dots, individual brains. Error bars, means ±95% confidence intervals.

Figure 4

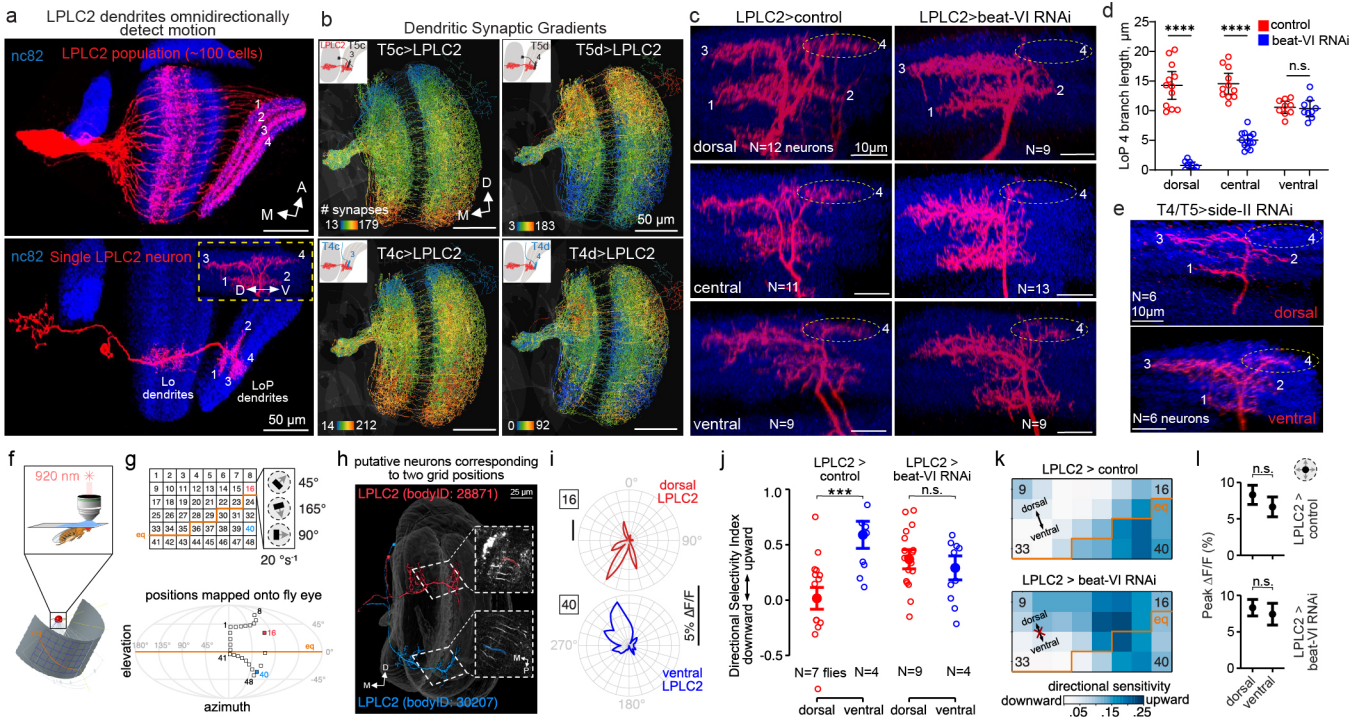
a
LPLC2 dendrites omnidirectionally detect motion
nc82
LPLC2 population (~100 cells)
nc82 Single LPLC2 neuron
Lo dendrites
LoP dendrites
50 µm
b
Dendritic Synaptic Gradients
T5c>LPLC2
T5d>LPLC2
T4c>LPLC2
T4d>LPLC2
synapses
13 179
3 183
14 212
0 92
50 µm
c
LPLC2>control
LPLC2>beat-VI RNAi
dorsal N=12 neurons
10µm
N=9
central N=11
N=13
ventral N=9
N=9
d
LoP 4 branch length, µm
control
beat-VI RNAi
****
****
n.s.
dorsal
central
ventral
e
T4/T5>side-II RNAi
N=6
10µm
dorsal
N=6 neurons
ventral
f
920 nm
g
45°
165°
90°
20 °s⁻¹
positions mapped onto fly eye
elevation
azimuth
h
putative neurons corresponding to two grid positions
LPLC2 (bodyID: 28871)
25 µm
LPLC2 (bodyID: 30207)
i
dorsal LPLC2
ventral LPLC2
5% ΔF/F
j
LPLC2 > control
LPLC2 > beat-VI RNAi
***
n.s.
Directional Selectivity Index downward ← → upward
N=7 flies
N=4
N=9
N=4
dorsal
ventral
dorsal
ventral
k
LPLC2 > control
LPLC2 > beat-VI RNAi
dorsal
ventral
eq
directional sensitivity
downward
upward
.05
.15
.25
l
n.s.
n.s.
Peak ΔF/F (%)
LPLC2 > control
LPLC2 > beat-VI RNAi
dorsal
ventral

1599 **Fig. 4: A gradient of Beat-VI::Side-II recognition molecules controls a motion**
1600 **detection synaptic gradient in LPLC2 neurons**
1601 **a-b, LPLC2 dendritic synaptic gradients**
1602 **a,** Confocal projections of the LPLC2 population (top) and an individual LPLC2
1603 neuron (bottom) in dorsal view, highlighting the dendritic branches in the lobula
1604 plate (LoP). Numbers, LoP layers. Inset: posterior view of a single LPLC2 LoP
1605 dendrite with branches extending into only one of the four cardinal directions in
1606 each layer. D, dorsal; V, ventral; M, medial; P, posterior.
1607 **b,** EM-based reconstructions (Flywire connectome) of LPLC2 neurons (posterior
1608 view), color-coded by the number of inputs each LPLC2 neuron receives from T4c,
1609 T4d, T5c and T5d neurons. Insets, schematics of single LPLC2 (red) and T4/T5c-
1610 d neurons, overlaid on lobula/lobula plate outlines.
1611 **c-e, beat-VI differentially regulates LPLC2 dendrites along the LoP4 DV axis.**
1612 **c,** Confocal projections of individual LoP dendrites (posterior view) in dorsal,
1613 central and ventral LPLC2 in control and LPLC2>beat-VI RNAi flies. Numbers, LoP
1614 layers. Dashed ovals, LoP4 dendritic branches.
1615 **d,** Length of LoP4 dendritic branches for dorsal, central and ventral LPLC2
1616 neurons in control and LPLC2>beat-VI RNAi flies. Dots, individual neurons. Error
1617 bars, means ±95% confidence intervals.
1618 **e,** Confocal projections of individual LoP dendrites (posterior view) of dorsal and
1619 ventral LPLC2 neurons in control and T4/T5>side-II RNAi flies. Dashed ovals,
1620 LoP4 dendritic branches.
1621 **f-l, beat-VI differentially regulates integration of motion by LPLC2 neurons**
1622 **f,** Schematic of the fly eye relative to the surrounding LED display for visual
1623 stimulation during two-photon calcium imaging.
1624 **g,** Positions on the LED display probing LPLC2 receptive field by presentation of
1625 dark edges moving in 24 (0° to 345°) different orientations (top). Yellow line, fly
1626 eye's equator (eq) projected onto the LED display. Mollweide projection of the
1627 outermost positions (black boxes) relative to the fly eye during Ca2+ imaging
1628 experiments (bottom).
1629 **h,** EM-based reconstructions of LPLC2 neurons stimulated by grid positions 16
1630 and 40 (see Methods). LPLC2 neurites viewed during Ca2+ imaging with single-
1631 cell regions of interest (color-coded by positions) overlaid on them (insets, scale
1632 bar: 10 μm).
1633 **i,** Polar plots of the peak responses to moving dark edges in dorsal and ventral
1634 LPLC2 neurons in a representative fly.
1635 **j,** Directional sensitivity index (DSI) for dorsal and ventral LPLC2 neurons in control
1636 and beat-VI RNAi flies. Dots, individual recordings. Error bars, means ±95%
1637 confidence intervals.
1638 **k,** Filtered heatmap of the DSI for all positions tested in control and beat-VI RNAi
1639 flies.
1640 **l,** Average peak responses to a looming stimulus above (dorsal) or below (ventral)
1641 the eye's equator in control and beat-VI RNAi flies. Error bars, means ±95%
1642 confidence intervals.
1643

Extended Data Figure 1 (related to Fig. 1)

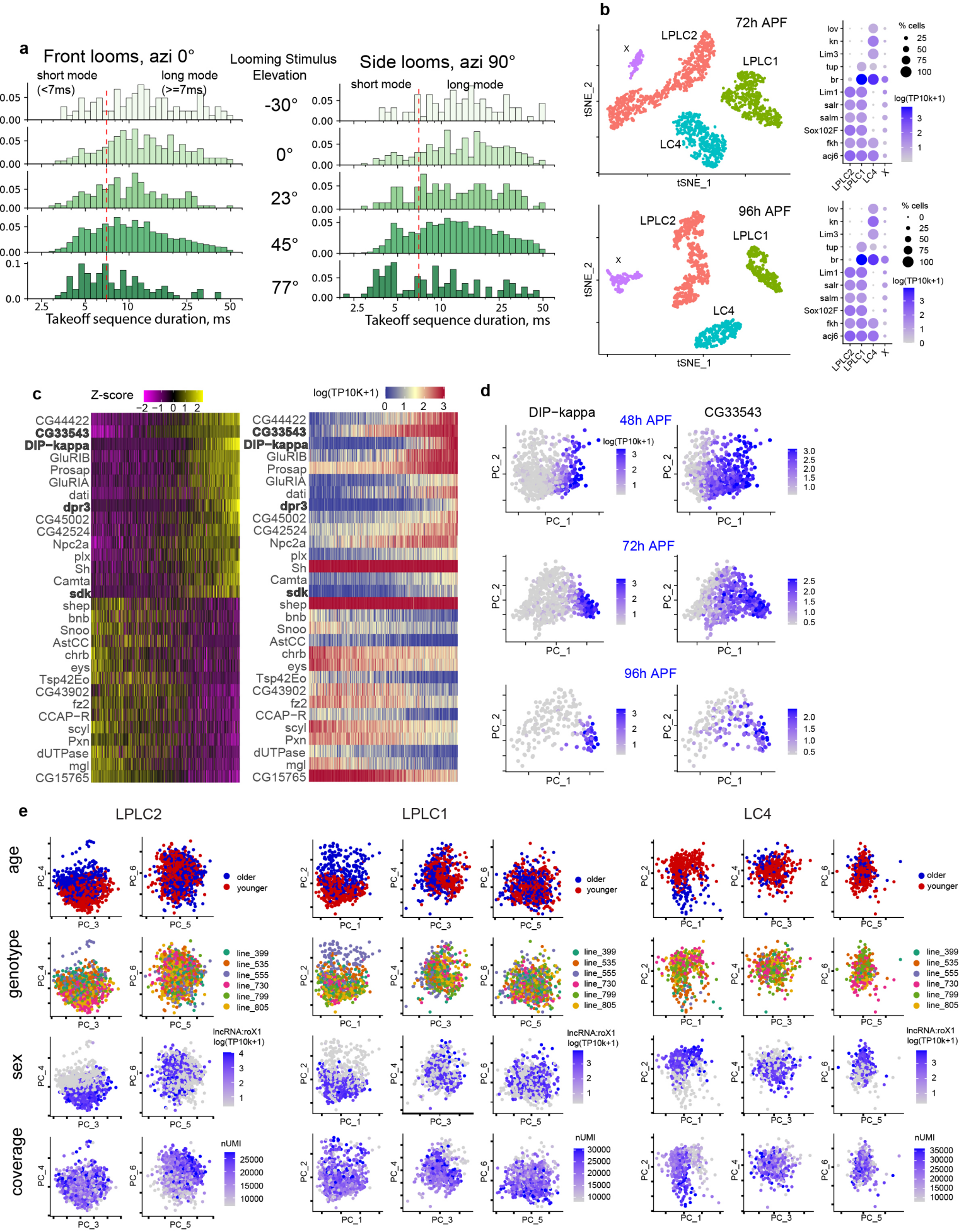

Extended Data Figure 1 (related to Fig. 1). Synaptic gradients are associated with molecular heterogeneity across VPN cell types

a, Histograms showing the distribution of takeoff sequence durations in response to frontal (left) and lateral (right) looming stimuli at different elevations (detailed breakdown of data summarized in Fig. 1e). Short-mode and long-mode takeoffs are distinguished by the red dashed lines.

b, t-SNE plots of 72h and 96h APF datasets (left). LPLC2, LPLC1, and LC4 neurons were annotated based on the expression of known transcription factors (right). X indicates unknown ectopic cell types.

c, Heatmaps of the expression patterns of the top 30 genes with the highest contribution (loading) to differentially expressed genes along Principal Component 1 (PC1) across LPLC1 neurons at 48h APF (see Fig. 1 legend for details). Genes encoding cell recognition molecules (IgSF superfamily) are highlighted in bold.

d, PCA plots of LPLC1 neurons at 48, 72, and 96h APF, colored by the expression levels of two cell recognition molecules from (**c**).

e, PCA plots of LPLC2, LPLC1, and LC4 neurons at 48h APF colored by genotype, age (early vs late collection), genotype (DGRP line), sex (male-specific transcript), and coverage. PC1-6 for LPLC1 and LC4, and PC3-6 for LPLC2 are shown.

Extended Data Figure 2 (related to Fig. 1)

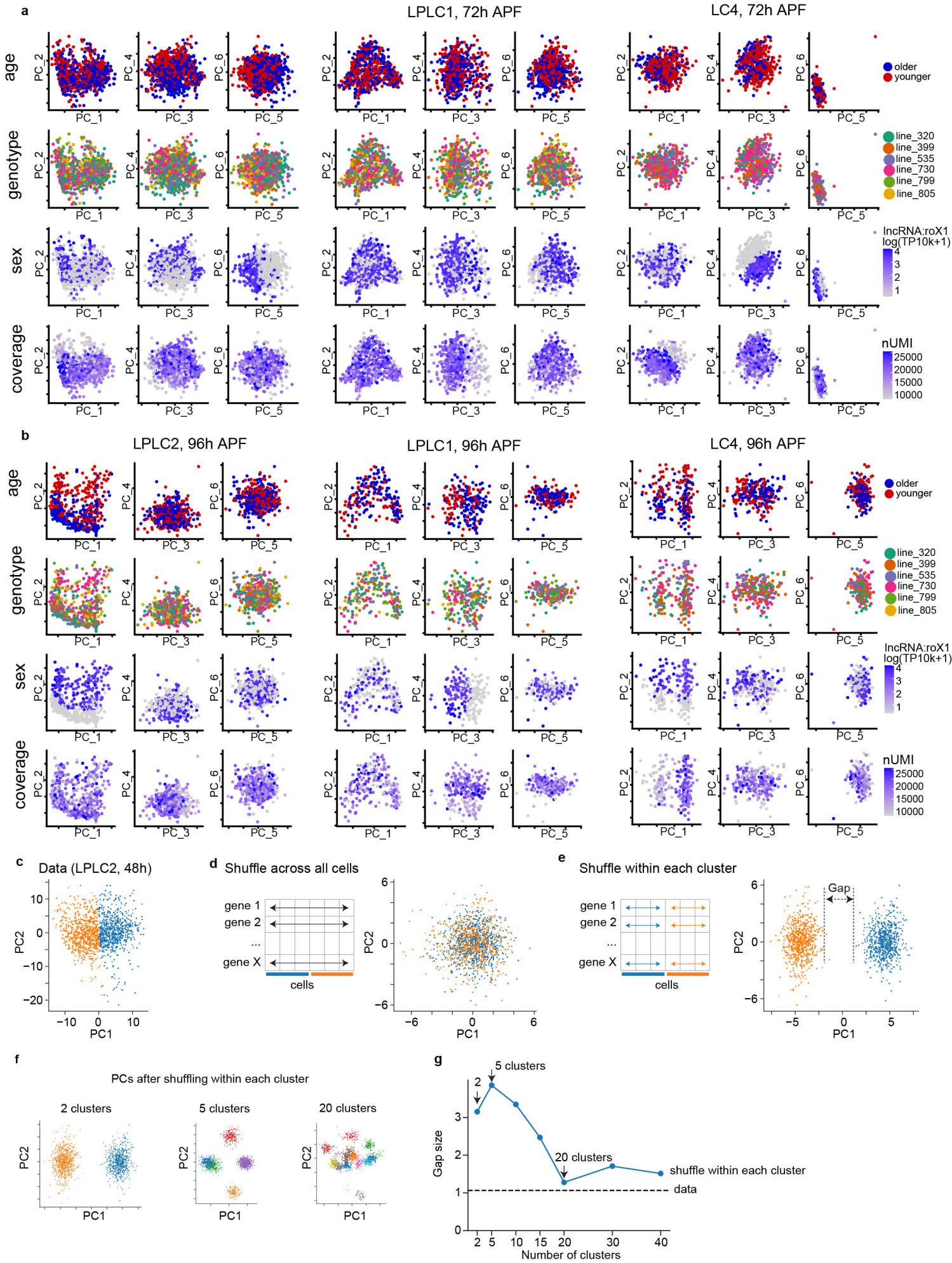

Extended Data Figure 2 (related to Fig. 1). Further analysis of within-cell-type heterogeneity in gene expression across LPLC2, LPLC1 and LC4

a-b, PCA plots of LPLC2, LPLC1 and LC4 neurons at 72h APF (**a**) and 96h APF (**b**) colored by genotype, age (early vs late collection), genotype (DGRP line), sex (male-specific transcript), and coverage. Shown are PC1-6.

c-e, Scatter plots of LPLC2 cells (48h APF) embedded in the first two principal components (PC1 and 2) colored by their cluster labels (n=2, inferred from K-means clustering). PCs are calculated using the top 1000 highly variable genes based on the actual data (**c**), after shuffling gene expression levels for each gene independently across all cells (**d**), and after shuffling each gene only within each cluster (**e**), respectively. Shuffling gene expression across all cells (**d**) disrupts this gradient, indicating that the observed differences reflect coordinated gene expression rather than uncorrelated variation. Shuffling within each cluster (**e**) disrupts the internal gradient of each cluster, creating artificial gaps not present in the original data (**c**), which suggests that the continuous gradient observed in the original data cannot be represented as a set of discrete clusters.

f, Scatter plots of cells in PCA embeddings after shuffling genes within each cluster for an increasing number of fine-grained clusters (n=2,5,30).

g, Gap size as a function of the number of clusters. Gap size is defined as the minimum distance in PC1 and PC2 space needed to connect 90% of cells into a single graph component. The gap size decreases and plateaus as the number of clusters increases. This means that a continuum can be approximated by a large number of discrete clusters. However, a small number of clusters (like 2) is insufficient to capture the continuous nature of the data.

Extended Data Figure 3 (related to Fig. 2)

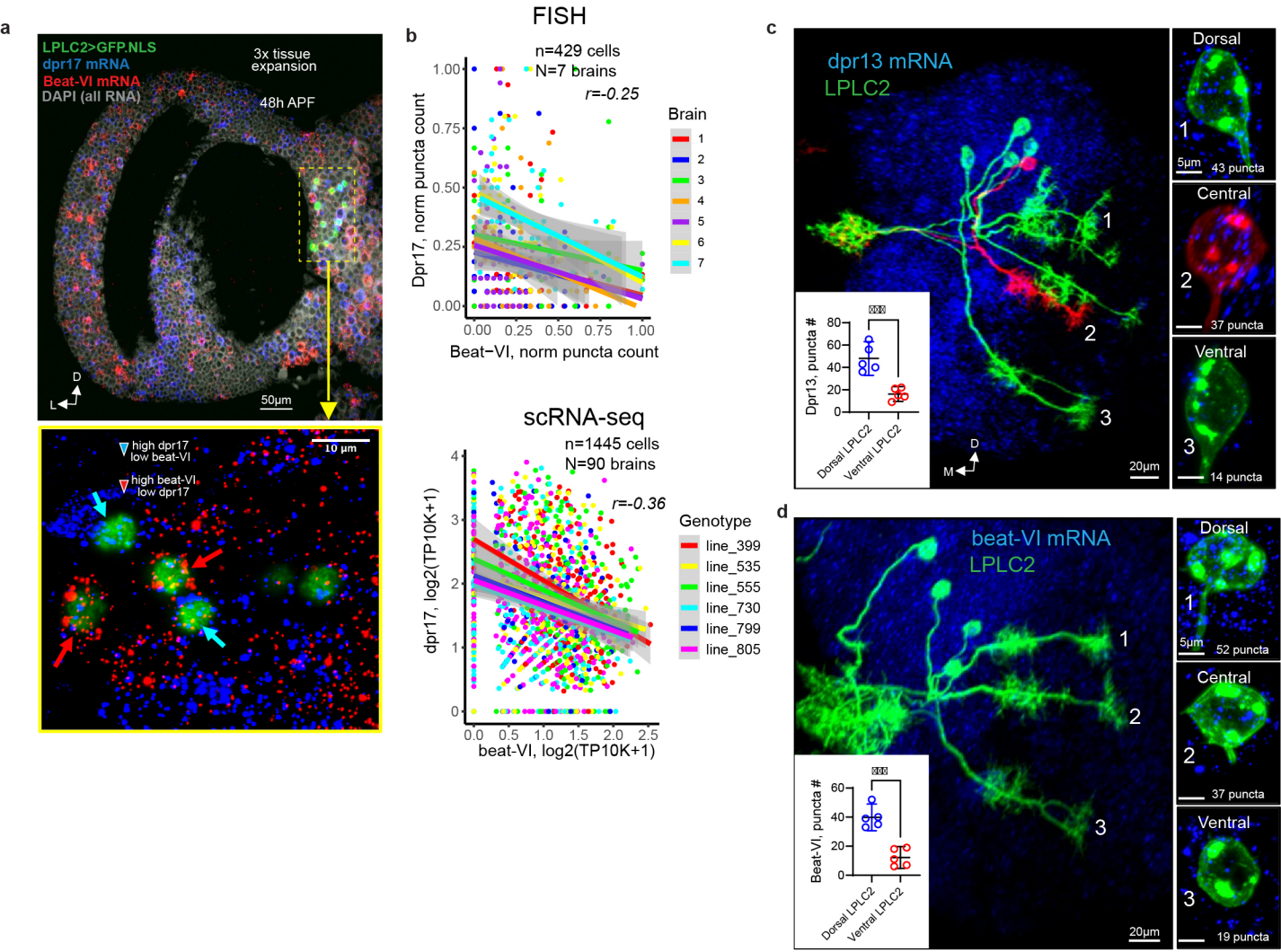

Extended Data Figure 3 (related to Fig. 2). HCR-FISH validates gradients of cell recognition molecules in LPLC2.

a, Light sheet projection of the expanded *Drosophila* optic lobe (48h APF) with labeled LPLC2 nuclei and transcripts of dpr17 and beat-VI (top) and a single slice (0.5μm) from the light sheet projection (bottom, zoomed into the yellow dashed rectangular region); arrows indicate individual LPLC2 somas expressing markedly different levels of dpr17 and beat-VI. D, dorsal; L, lateral.

b, Comparison of scRNA-seq (top) and HCR-FISH (bottom) measuring the correlation in expression for dpr17 and beat-VI across LPLC2 neurons at 48h APF. Fitted lines represent the linear relationship between the two genes for each brain (FISH) or each wild type genotype (scRNA-seq); shaded regions represent 95% confidence intervals. r, Spearman's rank correlation coefficient.

c, dpr13 expression levels using HCR-FISH in individual sparsely labeled LPLC2 neurons. Right, zoomed-in cell bodies of dorsal, ventral, and central LPLC2 neurons, indicating the number of dpr13 transcripts per cell. Inset, comparison of dpr13 puncta counts in dorsal and ventral LPLC2 neurons. Dots represent individual neurons (1 neuron per brain). Error bars represent means ±95% confidence intervals.

d, Same as in (**c**), for beat-VI

Extended Data Figure 4 (related to Fig. 2)

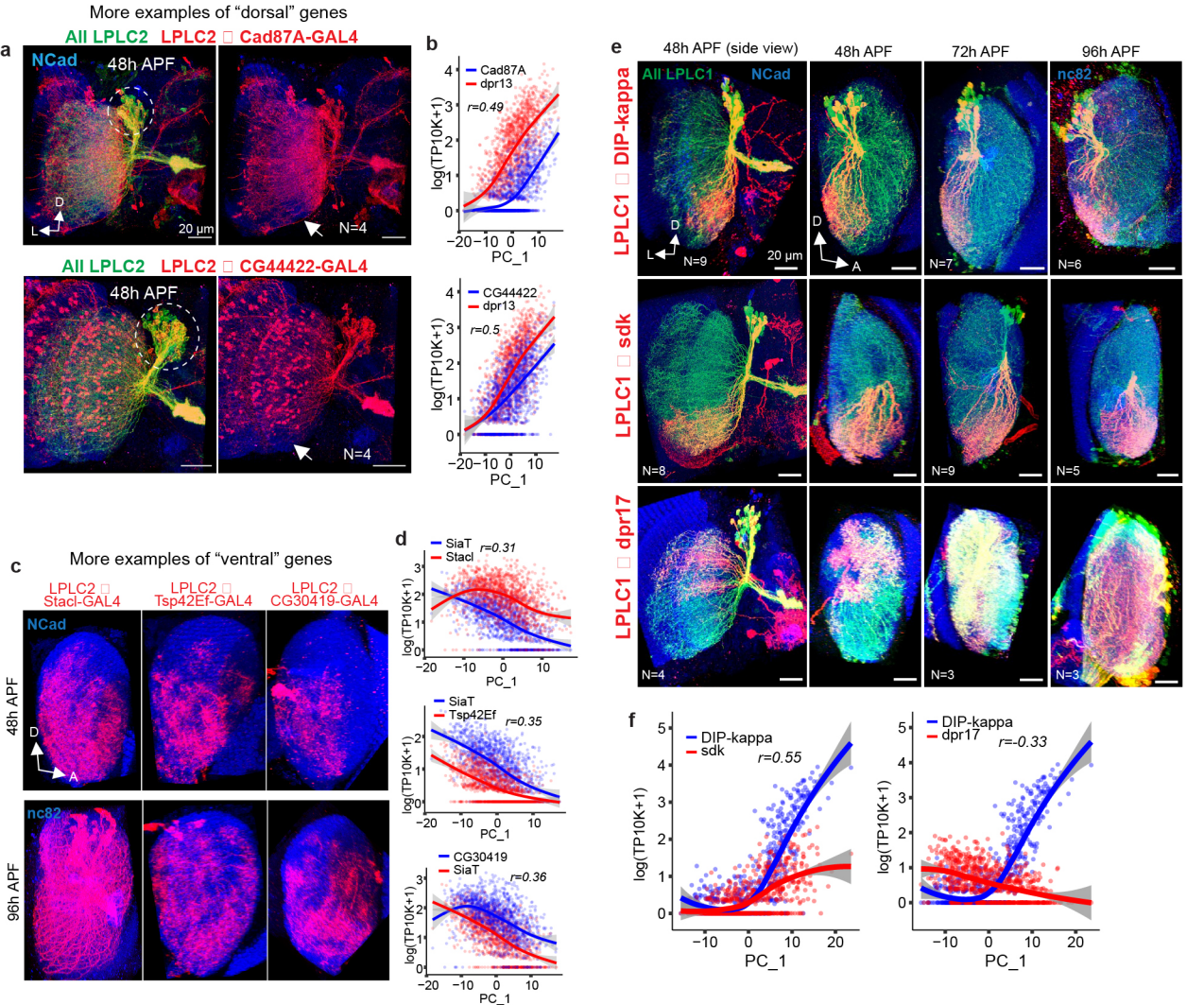

Extended Data Figure 4 (related to Fig. 2). Retinotopic correlates of molecular gradients in LPLC2 and LPLC1

a, Subsets of LPLC2 neurons expressing CG44422 and Cad87A at 48h APF. White arrows indicate ventral regions of the lobula lacking expression of both CG44422 and Cad87A. Dashed ovals, partial overlap of expression in somas, i.e., different LPLC2 neurons express different levels of CG44422 and Cad87A. N, number of brains tested. D, dorsal; L, lateral.

b, Positive correlation between expression levels of Cad87A, CG44422 and dpr13 (inferred from scRNA-seq), along PC1 across the LPLC2 population at 48h APF, indicating that both CG44422 and Cad87A can be considered “dorsal” genes.

c, Additional examples of genes expressed by ventral subpopulation of LPLC2 neurons. Red, dendrites of LPLC2 (lateral view of the lobula) that express stacl, Tsp42Ef and CG30419 at 48h (top) and 96h (bottom) APF. D, dorsal; P, posterior.

d, Positive correlation between expression levels of stacl, Tsp42Ef and CG30419 (inferred from scRNA-seq), along PC1 across the LPLC2 population at 48h APF.

e, Retinotopically biased gene expression across LPLC1 neurons. Red, subsets of LPLC1 neurons expressing DIP-kappa, sdk and dpr17 throughout development (posterior and lateral views of the lobula). N, number of brains tested. D, dorsal; M, medial; P, posterior.

f, Positive correlation between expression levels of DIP-kappa and sdk (top), and negative correlation between expression levels of DIP-kappa and dpr17 (bottom), (inferred from scRNA-seq), along PC1 across the LPLC1 population at 48h APF, reflecting the retinotopically biased expression of these genes in (**e**).

Extended Data Figure 5 (related to Fig. 3)

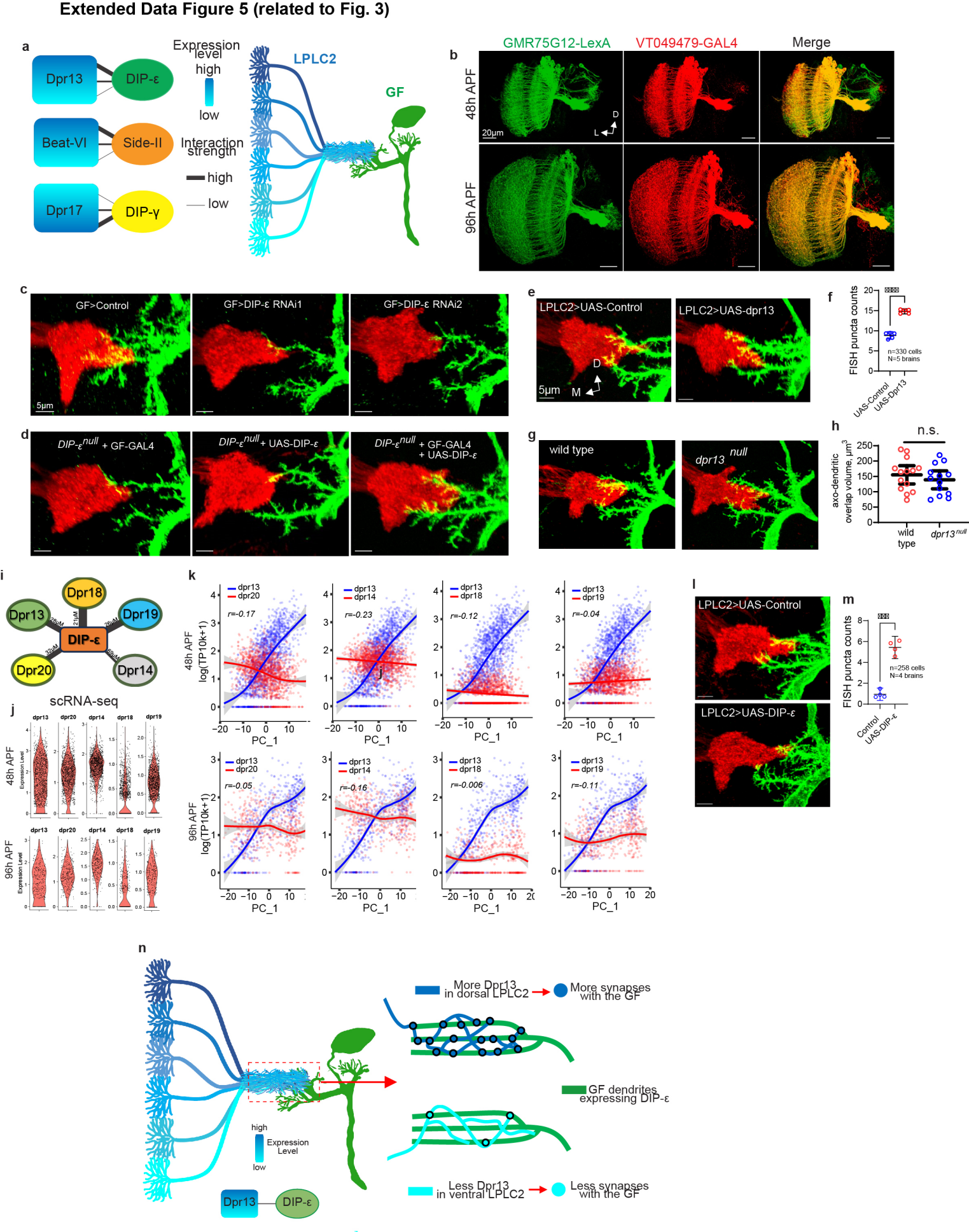

Extended Data Figure 5 (related to Fig. 3). Synaptic gradient between LPLC2 and the GF is established through a gradient of DIP-ε::Dpr13 molecular interactions.

a, To establish a synaptic gradient with LPLC2 based on dorsoventral expression gradient of any of the candidate molecules (Dpr13, Beat-VI, Dpr17), the GF needs to express a molecular binding partner to recognize one or more of these molecules.

b, Validation of VT049479-GAL4 expression in LPLC2 using GMR75G12-LexA as a reference. A complete overlap confirms that VT049479-GAL4 targets the entire LPLC2 population. D, dorsal; M, medial.

c, Confocal projections of LPLC2 axon terminals and Giant Fiber dendrites in wild-type animals, as well as animals expressing control RNAi and two different DIP-ε RNAi in the Giant Fiber.

d, Same as (**c**). Rescue experiment: overexpression of DIP-ε cDNA in the GF in *DIP-ε^{null}* background (right) compared to two negative controls (left and middle).

e, Confocal projections of LPLC2 axon terminals and the Giant Fiber dendrites in control animals and animals overexpressing dpr13 in LPLC2

f, Comparison of dpr13 mRNA levels in LPLC2 (assessed using HCR-FISH) in control animals and animals overexpressing dpr13. Dots, individual brains. Error bars, means ±95% confidence intervals.

g-h, Confocal projections of LPLC2 axon terminals and the Giant Fiber dendrites in wild type and *dpr13^{null}* animals **(g)** and comparison of axo-dendritic overlap volume between LPLC2 and the GF for these conditions **(h)**; Dots, individual brains. Error bars, means ±95% confidence intervals.

i, Protein interaction map showing binding strength (affinity values are inversely proportional to edge thickness) between DIP-ε and multiple Dprs expressed in LPLC2.

j, expression levels of DIP-ε binding Dprs in LPLC2 at 48h and 96h APF (inferred from scRNA-seq data generated in this study).

k, Correlation between expression levels of dpr13 and other DIP-ε binding dprs in LPLC2 at 48h and 96h APF (inferred from scRNA-seq), along PC1 across the LPLC2 population at 48h and 96h APF.

l-m, Confocal projections of LPLC2 axon terminals and the Giant Fiber dendrites in control animals and animals overexpressing DIP-ε in LPLC2 (**l**) and comparison of axo-dendritic overlap volume between LPLC2 and the GF for these conditions (**m**); dots, individual brains. Error bars, means ±95% confidence intervals.

n, Suggested model: a dorsoventral gradient of dpr13 expression across LPLC2 population determines how many synapses each LPLC2 axon will make with the GF via binding with DIP-ε on the GF dendrites.

Extended Data Figure 6 (related to Fig. 3)

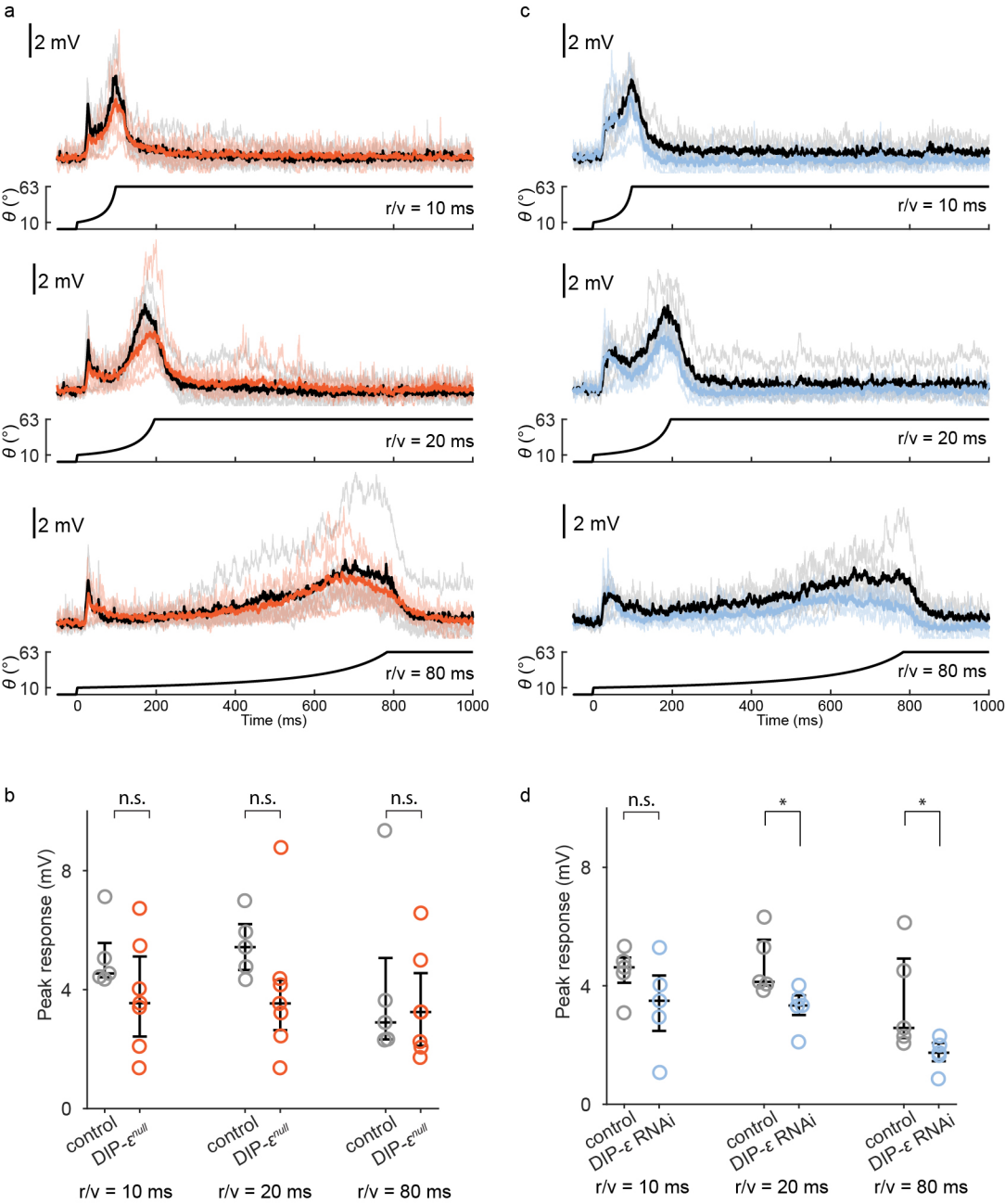

Extended Data Figure 6 (related to Fig. 3). Electrophysiology of the GF

a, GF responses to looming stimuli, in r/v = 10ms (top), r/v = 20ms (middle), r/v = 80ms (bottom). Control (average: black, individual fly: grey) and *DIP-ε*^{null} (average: orange, individual fly: light orange) traces are overlayed. Looming stimulus profile over time is displayed below the GF responses.

b, Quantification of expansion peak amplitudes in (**a**) from individual flies.

c, Same as (**a**) for controls (grey) and animals overexpressing DIP-ε RNAi in the GF (light blue).

d, Quantification of expansion peak amplitudes in (**c**) from individual flies.

Extended Data Figure 7 (related to Fig. 3)

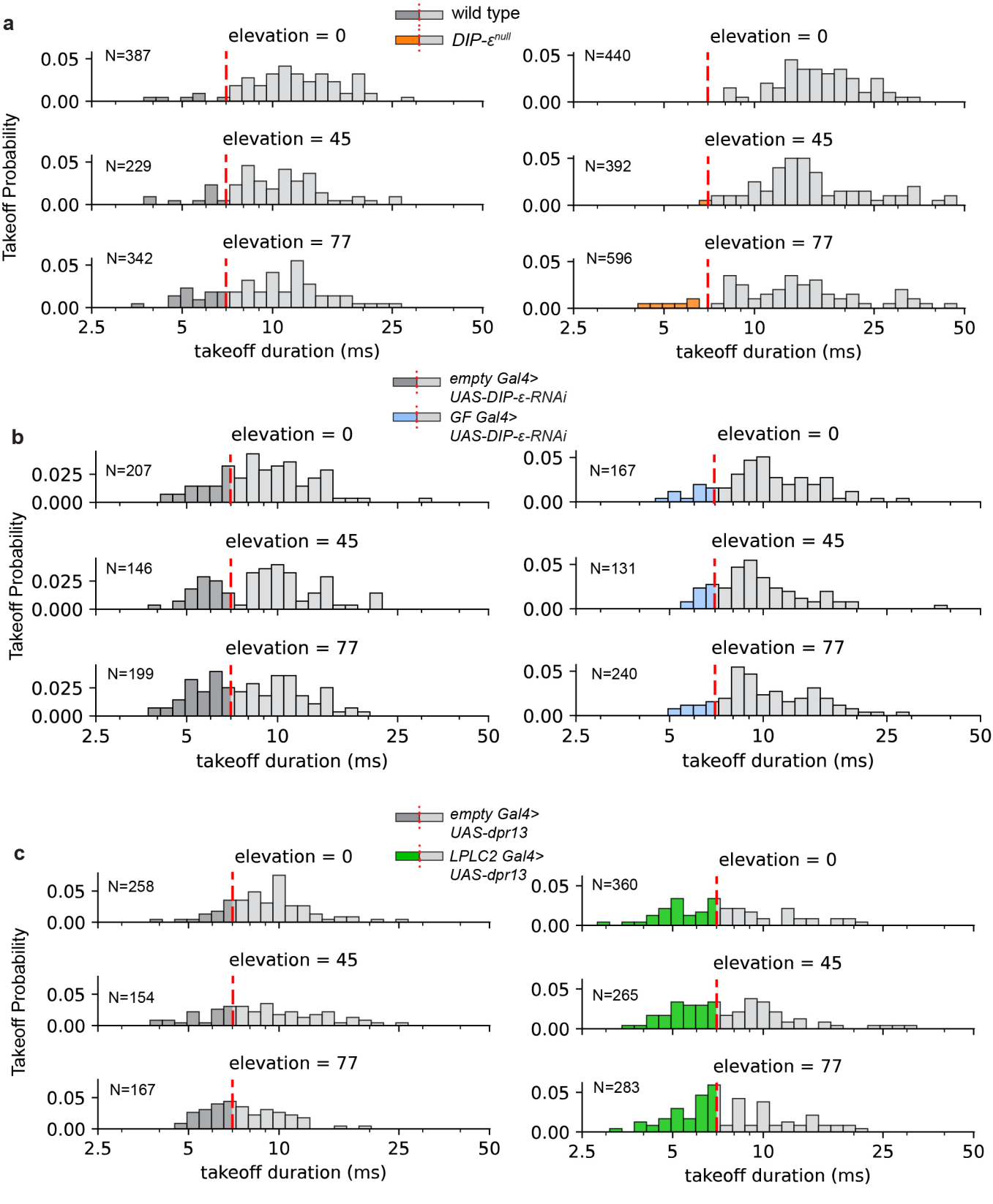

Extended Data Figure 7 (related to Fig. 3). Functional relevance of DIP-ε::Dpr13 molecular gradient regulating the LPLC2-GF synaptic gradient.

a, Histograms showing the distribution of takeoff sequence durations at different stimulus elevations (0°, 45°, and 77°) in wild-type (left, grey) and *DIP-ε^{null}* flies (right, orange). Short-mode and long-mode takeoffs are distinguished by red dashed lines. N, number of flies that performed a takeoff.

b, Same as (**a**) for controls (empty-Gal4 driving DIP-ε RNAi expression, left, grey) and flies expressing DIP-ε RNAi in the GF (right, blue).

c, Same as (**a**) for controls (empty-Gal4 driving expression of dpr13, left, grey) and flies overexpressing dpr13 in LPLC2 neurons (right, green).

Extended Data Figure 8 – related to Figure 4

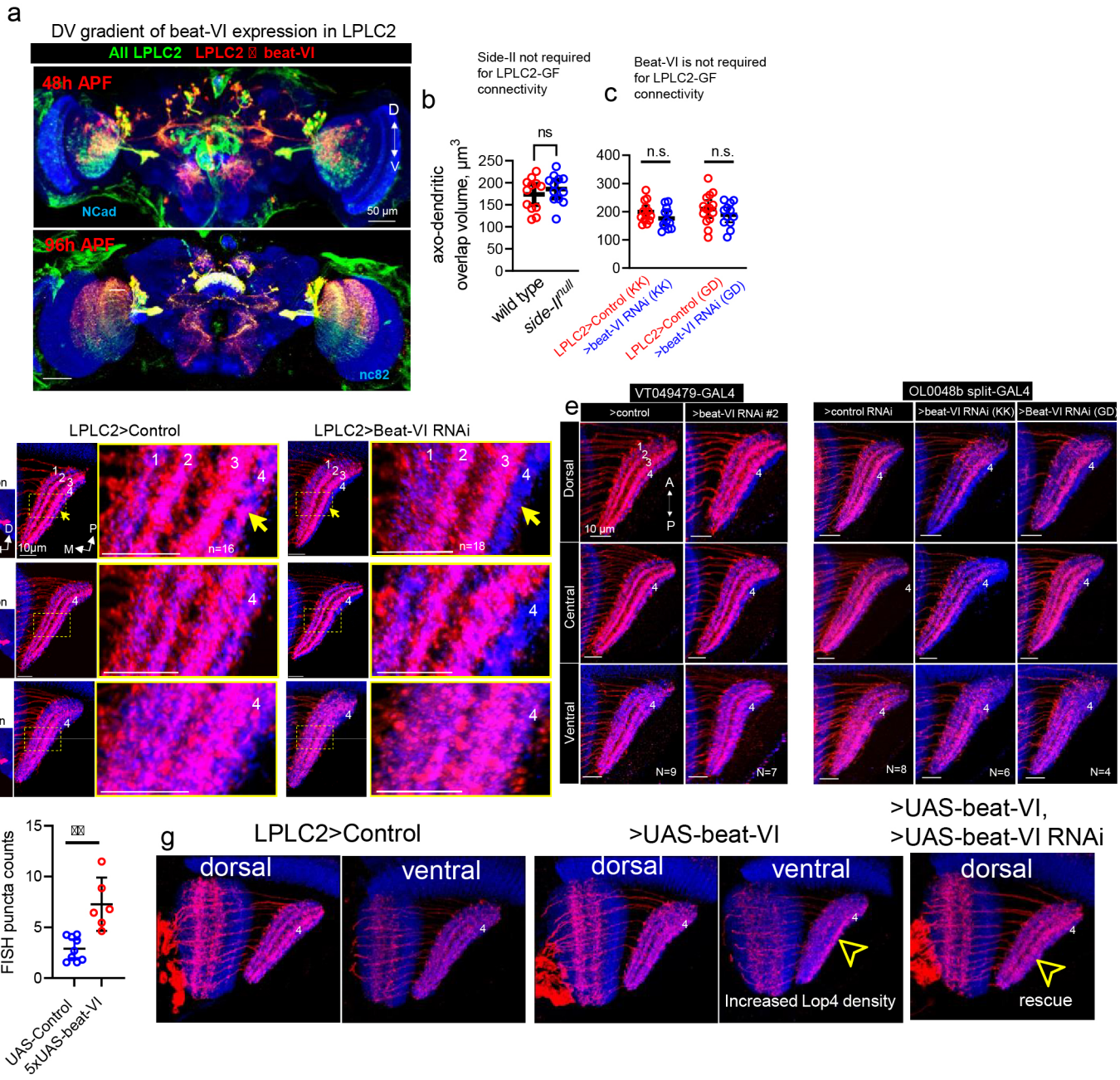

Extended Data Figure 8 (related to Fig. 4). Graded expression of Beat-VI across LPLC2 neurons differentially affects the LoP4 dendritic wiring.

a, Dorsally biased expression of beat-VI across LPLC2 population. Red, subsets of LPLC2 neurons expressing beat-VI at 48h APF (top) and 96h APF (bottom). Green, all LPCL2 neurons. D, dorsal; V, ventral.

b-c, Comparison of axo-dendritic overlap volume between LPLC2 and the GF in *side-II*^{null} animals (**b**), and in animals with LPLC2 expressing beat-VI RNAi (**c**). Dots, individual brains. Error bars, means ±95% confidence intervals.

d, Confocal projections of LPLC2 dendrites (entire LPLC2 population labeled) in the lobula plate in control animals (left) and in animals with beat-VI RNAi expressed in LPLC2 (riht). Leftmost panels, posterior views of the LPLC2 population with dashed rectangles indicating the location of cross-sections for dorsal, central, and ventral subsets of LPLC2. Numbers indicate LoP layers. Yellow arrows indicate LoP4 layer. D, dorsal; M, medial; L, lateral; P, posterior.

e, Same as (**d**) for two different LPLC2 GAL4 driver lines and two different beat-VI RNAi lines.

f, Comparison of beat-VI mRNA levels in LPLC2 (assessed using HCR-FISH) in control animals and animals overexpressing beat-VI in LPLC2. Dots, individual brains. Error bars, means ±95% confidence intervals.

g, Confocal projections of LPLC2 dendrites (entire LPLC2 population labeled, dorsal and ventral cross-sections compared) in the lobula plate in control animals (left), animals overexpressing beat-VI cDNA (middle), and animals overexpressing beat-VI cDNA while also expressing beat-VI RNAi (right). Yellow arrowheads indicate a change in LoP4 dendritic density.

Extended Data Figure 9 (related to Fig. 4)

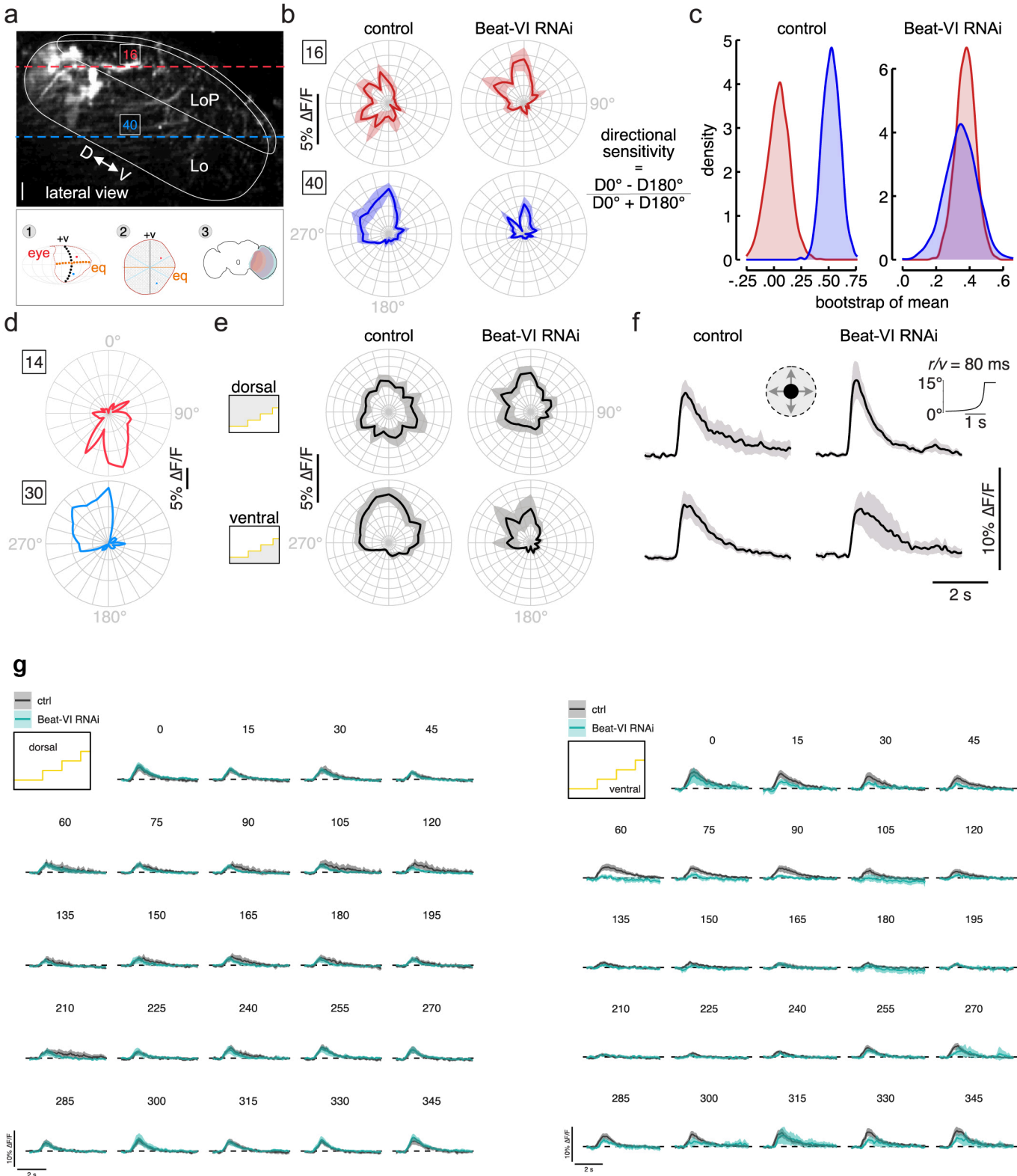

Extended Data Figure 9 (related to Fig. 4). Beat-VI::Side-II molecular gradient regulates LPLC2-T4d/T5d synaptic gradient.

a, 3D reconstruction of LPLC2 neurons from a Z-stack taken using the two-photon microscope in a head-fixed fly (lateral view, scale bar: 10 μm). Dashed lines highlight the two Z-planes where LPLC2 dendrites responded to dark looming at positions 16 (red) and 40 (blue) on the LED display (top). White solid lines approximately define the reference neuropils. Schematic of the procedure used to identify the putative neurons in the fly connectome stimulated by two representative grid positions (bottom, see Methods).

b, Polar plots of the average peak responses to moving dark edges in dorsal (16) and ventral (40) regions (color-coded by position) for control and beat-VI RNAi flies. Error band, s.e.m.

c, Bootstrap of the mean of the directional sensitivity ratio in dorsal (16) and ventral (40) regions (color-coded by position) for control and beat-VI RNAi flies (10,000 repetitions).

d, Polar plots of the peak responses to moving dark edges in dorsal (14) and ventral (30) regions in two representative flies (color-coded by position).

e, Polar plots of the average peak responses to moving dark edges in aggregated dorsal (above the equator) and ventral (below the equator) regions for control and beat-VI RNAi flies. Error band, s.e.m.

f, Average calcium transient in response to a dark looming in dorsal (above the equator) and ventral (below the equator) regions for control and beat-VI RNAi flies. Error band, s.e.m.

g, Average calcium transients in response to dark edges moving in 24 (from 0° to 345°) different orientations for control and LPLC2>beat-VI RNAi flies. Dorsal (left) and ventral (right) regions. Error band, s.e.m.